Article

Developmental Cell

Primary Cilia Signaling Promotes Axonal Tract Development and Is Disrupted in Joubert Syndrome-Related Disorders Models

Graphical Abstract

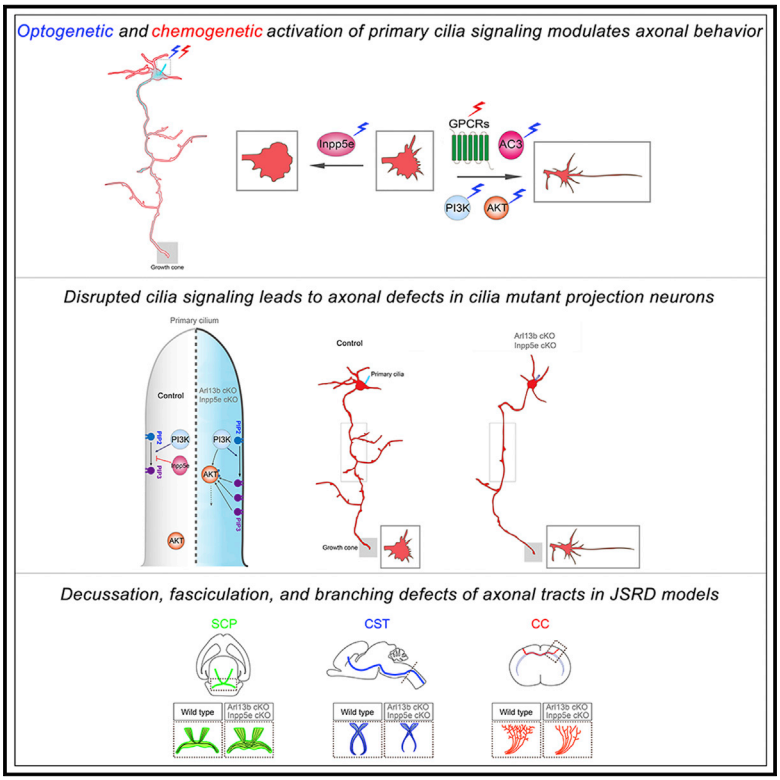

Highlights

- Chemogenetic and/or optogenetic activation of primary cilia alters axonal behavior
- Ciliary activity modulates axonal growth cones and filopodial-lamellipodial balance
- Arl13b-Inpp5e activity in cilia facilitates axonal tract formation and targeting
- Disrupted ciliary signaling contributes to axonal tract malformations in JSRD

Authors

Jiami Guo, James M. Otis, Sarah K. Suciu, ..., Garret D. Stuber, Tamara Caspary, E.S. Anton

Correspondence

jiami.guo@ucalgary.ca (J.G.), tcaspar@emory.edu (T.C.), anton@med.unc.edu (E.S.A.)

In Brief

Guo et al. show that primary cilia-driven signaling regulates growth cone dynamics and axonal tract development. Ciliary signaling receptor activation and associated changes in signaling cascades (PI3K, AKT, and AC3) and transcriptional landscape affect axons. Disrupted ciliary signaling following mutations in Arl13b or Inpp5e leads to axonal tract malformations in JSRD.

Guo et al., 2019, Developmental Cell *51*, 759–774
December 16, 2019
https://doi.org/10.1016/j.devcel.2019.11.005

CellPress

Developmental Cell
Article

Primary Cilia Signaling Promotes Axonal Tract Development and Is Disrupted in Joubert Syndrome-Related Disorders Models

Jiami Guo,[1,2,*] James M. Otis,[1,7] Sarah K. Suciu,[3,7] Christy Catalano,[2,7] Lei Xing,[1] Sandii Constable,[3] Dagmar Wachten,[4] Stephanie Gupton,[1] Janice Lee,[1] Amelia Lee,[1] Katherine H. Blackley,[1] Travis Ptacek,[1] Jeremy M. Simon,[1] Stephane Schurmans,[5] Garret D. Stuber,[6] Tamara Caspary,[3,*] and E.S. Anton[1,8,*]

[1]UNC Neuroscience Center and the Department of Cell and Molecular Physiology, University of North Carolina School of Medicine, Chapel Hill, NC 27599, USA
[2]Hotchkiss Brain Institute and the Department of Cell Biology and Anatomy, University of Calgary, Calgary, AB T2N 4N1, USA
[3]Department of Human Genetics, Emory University School of Medicine, Atlanta, GA 30322, USA
[4]Biophysical Imaging, Institute of Innate Immunity, University Hospital Bonn, University of Bonn, Bonn, Germany
[5]Laboratory of Functional Genetics, GIGA Research Center, University of Liège, Liège, Belgium
[6]Center for the Neurobiology of Addiction, Pain and Emotion, Department of Anesthesiology and Pain Medicine, University of Washington, Seattle, WA 98195, USA
[7]These authors contributed equally
[8]Lead Contact
*Correspondence: jiami.guo@ucalgary.ca (J.G.), tcaspar@emory.edu (T.C.), anton@med.unc.edu (E.S.A.)
https://doi.org/10.1016/j.devcel.2019.11.005

SUMMARY

Appropriate axonal growth and connectivity are essential for functional wiring of the brain. Joubert syndrome-related disorders (JSRD), a group of ciliopathies in which mutations disrupt primary cilia function, are characterized by axonal tract malformations. However, little is known about how cilia-driven signaling regulates axonal growth and connectivity. We demonstrate that the deletion of related JSRD genes, *Arl13b* and *Inpp5e*, in projection neurons leads to de-fasciculated and misoriented axonal tracts. *Arl13b* deletion disrupts the function of its downstream effector, Inpp5e, and deregulates ciliary-PI3K/AKT signaling. Chemogenetic activation of ciliary GPCR signaling and cilia-specific optogenetic modulation of downstream second messenger cascades (PI3K, AKT, and AC3) commonly regulated by ciliary signaling receptors induce rapid changes in axonal dynamics. Further, *Arl13b* deletion leads to changes in transcriptional landscape associated with dysregulated PI3K/AKT signaling. These data suggest that ciliary signaling acts to modulate axonal connectivity and that impaired primary cilia signaling underlies axonal tract defects in JSRD.

INTRODUCTION

Primary cilia are present on virtually all cell types and, when defective, can lead to ciliopathies, occurring on the order of ~1:10,000 live births in the general population. A diagnostic feature of many ciliopathies is axonal tract defects (Green et al., 2018; Guadiana et al., 2013; Guemez-Gamboa et al., 2014; Hildebrandt et al., 2011; Reiter and Leroux, 2017; Sarkisian and Guadiana, 2015; Parisi, 2019; Poretti et al., 2007). Appropriate axonal growth and pathfinding are essential for wiring the developing brain (Chédotal and Richards, 2010; Engle, 2010). Axonal tract phenotypes in ciliopathies imply a role for primary cilia in axonal development and connectivity, but it is unclear how cilia-driven signaling emanating from near the neuronal soma acts to regulate axonal growth and connectivity.

Joubert syndrome-related disorders (JSRD), a prominent collection of ciliopathies, are autosomal recessive, congenital disorders with a variety of neurological symptoms including developmental delay, intellectual disabilities (ID), abnormal respiratory rhythms, hypotonia, ataxia, oculomotor apraxia, and mirror movement synkinesis (Parisi, 2019). The diagnostic feature of JSRD is the axonal tract malformation called the molar tooth sign (MTS), which presents as thickened, elongated, and horizontally orientated superior cerebellar peduncles (SCPs) that fail to decussate in the midbrain (Brancati et al., 2010; Juric-Sekhar et al., 2012; Parisi, 2019; Parisi and Glass, 2019; Romani et al., 2013; Sattar and Gleeson, 2011; Senocak et al., 2010). In addition to SCP malformation, absent or reduced decussation of the corticospinal tract (CST), corpus callosum (CC), and central pontine tracts are frequently observed in JSRD patients. Consistent with these axonal anomalies and the resultant changes in brain wiring, JSRD patients are often diagnosed with intellectual disabilities and autism spectrum disorder (ASD) (Marley and von Zastrow, 2012; Novarino et al., 2011; Reiter and Leroux, 2017).

Causative mutations for JSRD have been identified in 30+ cilia-related genes (Reiter and Leroux, 2017), implying a role for primary cilia in axon growth and guidance. To understand the role of primary cilia in axonal development and connectivity in the context of JSRD, we examined the function of two interrelated JSRD genes *ARL13B* (*JBTS8*, a small GTPase) and *INPP5E* (*JBTS1*, a phosphoinositide 5-phosphatase),

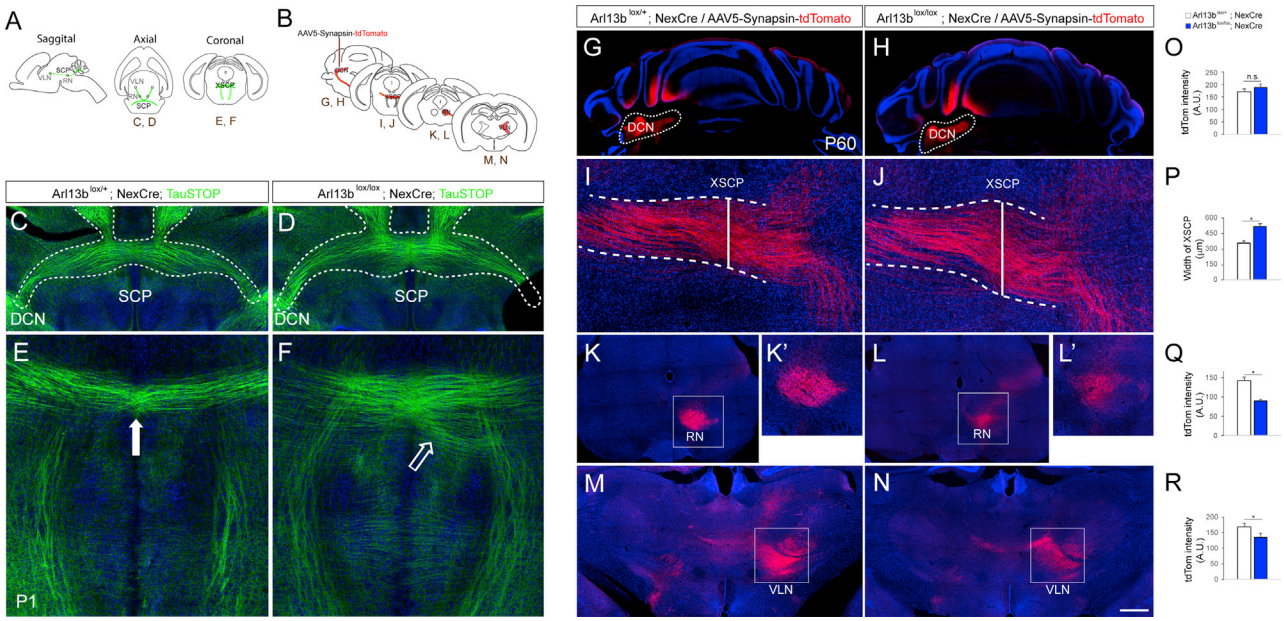

Figure 1. Deletion of *Arl13b* Leads to SCP Axonal Tract Defects

(A) Schematic of SCP tract in sagittal (left), axial (middle), and coronal (right) sections.

(B) Schematic of SCP axonal projection labeling by unilateral injection of AAV5-Synapsin-tdTom into the DCN.

(C and D) GFP labeling shows "x" shaped SCP tract (outlined in white dashed line) in *Arl13b$^{lox/+}$; NexCre; Taustop* (C) and *Arl13b$^{lox/lox}$; NexCre; Taustop* (D) axial sections.

(E and F) GFP labeling show SCP tract in *Arl13b$^{lox/+}$; NexCre; Taustop* (E) and *Arl13b$^{lox/lox}$; NexCre*; *Taustop* (F) in coronal sections (P1). White arrow (E) points to SCP decussation in control. Arrow (F) points to diffused, misoriented axons of SCP in *Arl13b$^{lox/lox}$; NexCre; Taustop* brains.

(G and H) Coronal cerebellar sections show tdTom$^+$ DCN neurons in *Arl13b$^{lox/+}$; NexCre* (G) and *Arl13b$^{lox/lox}$; NexCre* (H) brains (P60). DCN is outlined with dotted lines.

(I and J) tdTom$^+$ SCP decussation is wider in mutants (*Arl13b$^{lox/+}$*; *NexCre* (I) and *Arl13b$^{lox/lox}$*; *NexCre* (J)). White dashed lines outline the width of SCP tract.

(K and L) tdTom$^+$ SCP axons innervate the RN. (K′ and L′) Higher magnification of the RN region (white box) in (K) and (L).

(M and N) The target projection pattern of SCP into VLN of the thalamus in control (M) and mutants (N).

(O) Quantification of tdTom fluorescence intensity in the DCN indicates no significant differences.

(P) Quantification of XSCP width.

(Q and R) Quantification of fluorescence density of tdTom$^+$ DCN axonal terminals in RN (Q) and VLN (R) indicates reduced projection in Arl13b cKO brains. Data shown are mean ± SEM (n = 4 brains per group). *p < 0.05 (Student's t test). DCN, deep cerebellar nuclei; SCP, superior cerebellar peduncle; RN, red nucleus; VLN, ventrolateral nucleus; XSCP, decussation of SCP. Scale bar: 425 μm (C and D); 142 μm (G and H), 238 μm (I and J), 832 μm (K and L), and 960 μm (M and N). See also Figure S3.

respectively, in axonal development. ARL13B complexes with INPP5E, localize to primary cilia and both are essential for ciliary function. ARL13B is known for regulating ciliary signaling receptor (e.g., GPCRs, PDGFRα, and Smo) localization, whereas INPP5E controls the phosphoinositide composition of ciliary membrane and thus receptor trafficking, localization, and downstream signaling cascade activation (e.g., PI3K [phosphoinositide 3-kinase]/AKT) (Barral et al., 2012; Bielas et al., 2009; Cantagrel et al., 2008; Caspary et al., 2007; Garcia-Gonzalo et al., 2015; Mariani et al., 2016; Nachury et al., 2010; Phua et al., 2017; Umberger and Caspary, 2015). Deletion of *Arl13b* or *Inpp5e* impairs the ability of the primary cilium to function as a signaling hub, thus, providing excellent molecular models to examine how cilia-driven signaling regulate axon growth and connectivity in normal and JSRD brains.

Here, using neuron-specific mouse genetic models of *Arl13b* and *Inpp5e*, related human mutations, and chemogenetic and optogenetic manipulation of primary cilia signaling, we demonstrate that ciliary signaling lies at the heart of appropriate patterns of axon tract development and connectivity.

RESULTS

Aberrant Axonal Pathway Development in *Arl13b* Mutants

To evaluate the effect of primary cilia in axonal development, *Nex-Cre* line was used to delete *Arl13b* in post-mitotic cortical projection and deep cerebellar neurons (Goebbels et al., 2006; Su et al., 2012). These projection neurons are ciliated (Figure S1). The Nex-Cre line enables Cre recombinase-mediated deletion of *Arl13b* allele in these neurons from E13.5 (Higginbotham et al., 2012). Cre-dependent *Tau^{mGFP}* or *Ai9* reporter lines were used to visualize axons with GFP or mRFP, respectively (Hippenmeyer et al., 2005; Madisen et al., 2010). Deletion of Arl13b did not affect the survival of cortical projection or deep cerebellar neurons (Figure S2).

SCP axons of the deep cerebellar nuclei (DCN) extend toward and decussate in the caudal half of the midbrain, pass below and lateral to the red nucleus in the rostral midbrain, innervate the red nucleus, and then extend rostrally to the ventrolateral nucleus (VLN) of the thalamus (Figures 1A and 1B). The initial outgrowth

of SCP from cerebellum is diffused in Arl13b mutants (*Arl13b*$^{lox/lox}$; *Nex-Cre*; *Tau*^{mGFP}) (Figures S3A–S3D). Decussating SCP axons exiting cerebellum in controls (*Arl13b* $^{lox/+}$; *NexCre*; *Tau*^{mGFP}) turn rostrally at 91° ± 2.4° angle, whereas in mutants, SCP turns with a significantly wider angle (118° ± 2.8°; Figures S3E and S3F), suggesting a less coalesced and horizontally oriented SCP projection. The decussating Arl13b-deficient SCP axonal bundles are wider, loosely fasciculated, and contain misoriented fibers (Figures 1C–1F; SCP width [axial]: control, 291 ± 17 μm, Arl13b cKO, 355 ± 12 μm; n = 6 brains per group). To examine the projection pattern of SCP, AAV5-Synapsin-tdTomato virus (Klapoetke et al., 2014) was unilaterally injected into the DCN of control and *Arl13b-NexCre* mutant mice to label DCN axons (Figures 1B, 1G, 1H, and 1O). Compared to control, the decussation of mutant SCP is wider (Figures 1I, 1J, and 1P), and the DCN axonal projection into RN (Figures 1K, 1K′, 1L, 1L′, and 1Q) and VLN is significantly reduced (Figures 1M, 1N, and 1R).

To examine other JSRD-relevant axonal tracts disrupted in Arl13b mutants, we analyzed the corticospinal tract (CST). At P1, pyramidal decussation of CST is markedly disrupted (Figures 2A–2E). Clearly decussating pyramidal axons were evident in control (Figures 2B and 2D, arrowheads) but were significantly reduced in *Arl13b*$^{lox/lox}$*; NexCre* brains (Figures 2C and 2E, arrows). Consistent with this, the density of axons, post-decussation, innervating the distal cervical spinal cord, is reduced in *Arl13b-NexCre* mutants (Figure 2F [arrowhead] and 2G [arrow]). Together, these results suggest that the NexCre deletion of *Arl13b* in post-mitotic cortical neurons leads to disrupted CST formation and decussation.

To assess the effect of Arl13b deletion in callosal projection neurons, we performed unilateral *in utero* electroporation (IUE) at E15.5 with CAG-Cre and CAG-EGFP plasmids leading to *Arl13b* deletion and GFP labeling of callosally projecting neurons of layers 2/3 (Figure 2H). Callosal axons were analyzed at P1, as they cross the cortical midline to form the corpus callosum (CC) (Figures 2I and 2J). Compared to controls, Arl13b-deficient axons are loosely organized, poorly fasciculated, and form a wider CC tract (Figures 2I, 2I′, 2J, and 2J′; midline width of CC tract: control (95.2 ± 1.2 μm), mutant (140.2 ± 4.4 μm), Student's t test, p = 6.2E−5, n = 4 brains). The midline crossing growth cones of Arl13b-deficient neurons also display longer filopodial projections compared to control neurons (Figures 2I″ and 2J″ [arrowhead]); mutant: 5.63 ± 0.22 μm, control: 2.31 ± 0.27 μm, Student's t test, p = 0.001, n = 16 neurons). At P21, as CC axons reach their targets, control CC axons extensively branch and innervate ipsilateral layer 5 and contralateral layers 2/3 and 5 (Figures 2M and 2O [asterisk]). In contrast, Arl13b-deficient CC displayed disorganized axons (Figures 2K and 2L) as well as reduced axonal branching and innervation of target layers (Figures 2N [asterisk], 2P [asterisk], 2Q, and 2R). Lastly, decussation defects were also evident in the pontine nuclei. Transverse pontine tegmental axons do not decussate normally and are misoriented (Figures S3G and S3H).

Thickened SCPs that show disorganized decussation, perturbed pyramidal axon decussation, and transverse pontine fiber defects are consistent with the axonal phenotypes seen in JSRD. Our observations suggest that *Arl13b* deletion in projection neurons disrupts axonal tract development in a manner consistent with human JSRD phenotype. Further, these results suggest that disruption of primary cilia signaling through the deletion of *Arl13b* disrupts the appropriate formation and connectivity of major axon tracts in the brain, including SCP, CST, and CC. We therefore sought to explore the relationship between cilia signaling and axonal development.

Deletion of *Arl13b* Leads to Altered Axon Growth Behavior

To examine developmental changes in patterns of axon growth in Arl13b-deficient neurons, we isolated and cultured Ai9^{+} DCN neurons from control and *Arl13b*$^{lox/lox}$*; Nex-Cre; Ai9* (Arl13b cKO) brains. Evaluation of different stages of neuronal polarization (Banker, 2018) after initial plating suggests that axon-dendritic polarization (Figure S4) or axon formation and outgrowth are not affected in the absence of Arl13b, but fewer and shorter lateral axonal branches were seen in Arl13b-deficient neurons (Figures 3A [arrowheads], 3B, and 3C). Live imaging indicates that control axonal branches arise along the main axonal shaft (Figure 3D [arrowheads], and 3E). Consistent with the reduced axonal branching observed, mutant DCN neuron axons showed significantly reduced formation and dynamics of axonal branching protrusions (Figures 3D and 3E). These results suggest defects in the initiation and extension of axonal branching in Arl13b-deficient neurons.

We also observed reduced dendritic outgrowth of mutant DCN neurons *in vitro* (Figure 3A; total dendritic length $_{[DIV3]}$: control (274.1 ± 12.9 μm), mutant (116.5 ± 10.0 μm), Student's t test, p = 2.34E−11; # of primary dendrites$_{[DIV3]}$: control (5.7 ± 0.3), mutant (3.1 ± 0.2), Student's t test, p = 2.58E−08, n = 16$_{[Control]}$, 17$_{[mutant]}$ neurons).

Compared to control DCN neuron growth cones that show characteristic lamellipodial veils in between dynamic filopodial extensions ($t_{1/2}$ [half lifetime] = 24.4 ± 1.3 s), Arl13b-deficient growth cones are smaller but have numerous longer filopodial protrusions (Figures 3F and 3G [arrowheads]) with significantly reduced dynamics ($t_{1/2}$ = 118.5 ± 3.3 s, Student's t test, p < 0.05, n = 12 cells). Further, Arl13b null (Arl13b$^{-/-}$) embryonic cortical neurons also show reduced axon branching and disrupted growth cone morphology (Figure S5). Axons of Ift88 null (Ift88$^{-/-}$) cortical neurons without primary cilia were similarly affected (Figure S5). Together, these *in vitro* observations suggest that in the absence of appropriate primary cilia signaling, axonal growth cone dynamics and the filopodia to lamellipodia balance are altered.

The fasciculation defects *in vivo* and the axonal branching and growth cone defects *in vitro* in Arl13b-deficient axons suggest that communication and interactions between axons as they branch and extend as fiber tracts may have been perturbed in cilia mutant neurons. Intercellular recognition through adhesion molecules such as protocadherins are essential for axon growth and fasciculation. Within the protocadherin family, Protocadherin-17 (Pcdh17) is highly expressed in cortical and DCN neurons. Recruitment of Pcdh17 to axon-axon contacts is thought to facilitate the fasciculation and collective extension of the developing SCP axons (Hayashi et al., 2014; Hoshina et al., 2013). We therefore examined if primary cilia signaling is necessary to recruit Pcdh17 to points of axonal contacts *in vitro*. Control or Arl13b-deficient cortical neurons labeled with either

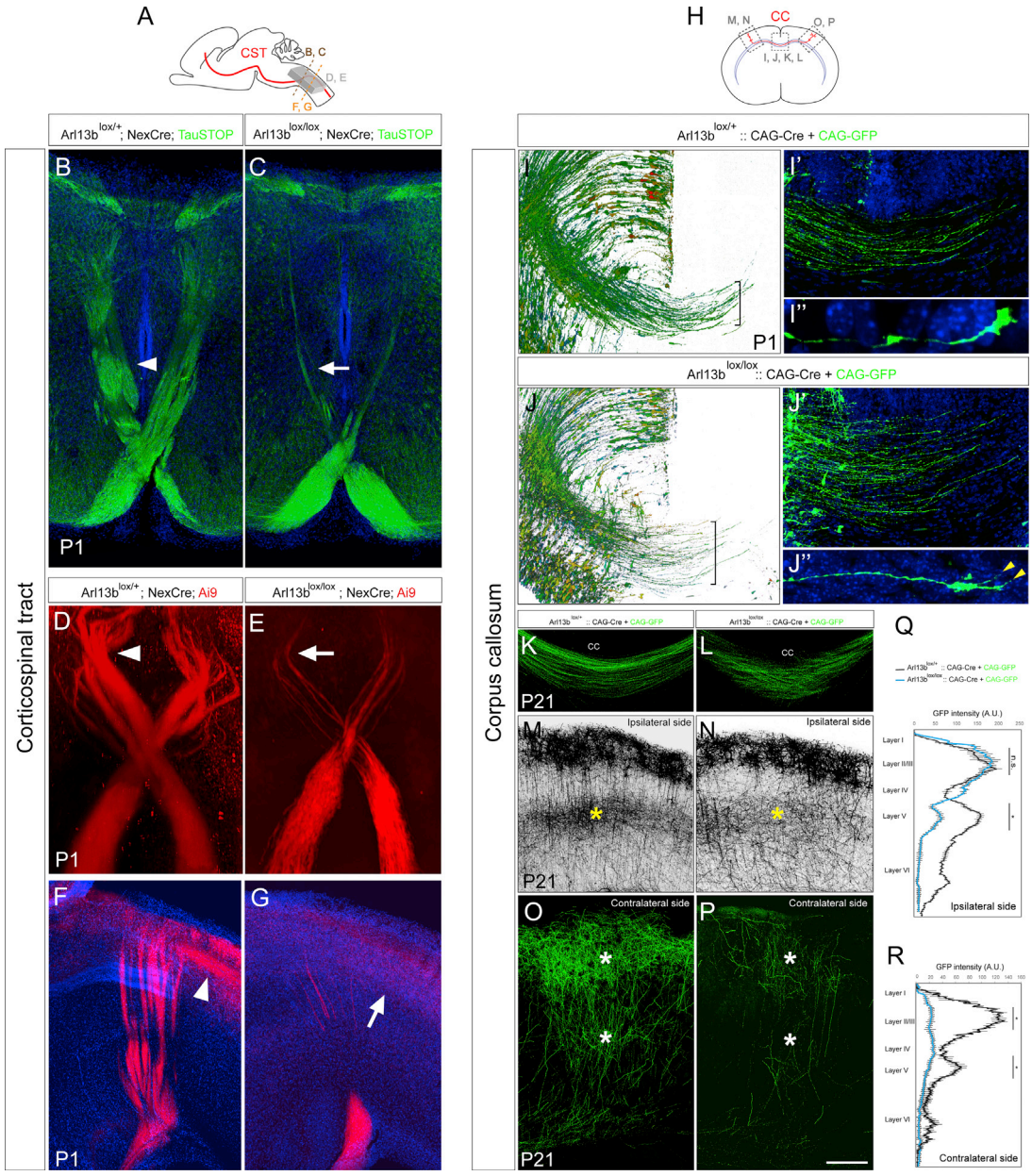

Figure 2. Deletion of *Arl13b* Leads to CST and CC Axonal Tracts Defects

(A) Schematic of CST tract in sagittal section. Dashed lines indicate where the CST decussation is and where (B and C) and (F and G) were imaged, respectively. Gray box indicates where (D) and (E) were imaged in cleared brains.

(B and C) GFP$^+$ CST tract decussation at lower medulla of *Arl13b$^{lox/+}$; NexCre; Taustop* (B, arrowhead) and *Arl13b$^{lox/lox}$; NexCre; Taustop* (C, arrow) brains (P1).

(D and E) CST decussation in cleared *Arl13b$^{lox/+}$; NexCre; Ai9* (D) and *Arl13b$^{lox/lox}$; NexCre; Ai9* (E) brains. Arrowhead (D) and arrow (E) point to the CST fascicles post-decussation.

(F and G) Sagittal sections of *Arl13b$^{lox/+}$; NexCre; Ai9* (F) and *Arl13b$^{lox/lox}$; NexCre; Ai9* (G) (P1) show reduced tdTom$^+$ CST tract fascicles post-decussation and the reduced extension of CST axons into the dorsal spinal cord in mutants (G, arrow; compare to control [F, arrowhead]).

(H) Schematic of CC tract in coronal section. Dashed rectangles indicate where (I–P) were imaged.

(I and J) *Arl13b$^{lox/+}$* (I) and *Arl13b$^{lox/lox}$* (J) embryos (E15) were electroporated with pCAG-Cre and pCAG-GFP plasmids. GFP labeled callosal axons in CC were analyzed at P1. Brackets indicate the width of CC. (I′ and J′) CC area highlighted in (I) and (J). (I″ and J″) Representative GFP$^+$ axonal growth cone of callosal neurons at the midline. Arrowheads point to longer filopodia in mutants.

(K–P) pCAG-Cre and pCAG-GFP electroporated *Arl13b$^{lox/+}$* (K, M, and O) and *Arl13b$^{lox/lox}$* (L, N, and P) embryos (E15) were analyzed at P21. GFP labeling show disorganized CC axons in *Arl13b$^{lox/lox}$* brains (L) electroporated with pCAG-Cre when compared to control (K). (M–P) Reduced axonal branching is evident in ipsilateral layer 5 (yellow asterisk, M, N) and contralateral layers 2/3 and 5 (white asterisks, O, P) in *Arl13b$^{lox/lox}$*; Cre brains.

(Q and R) Quantification of GFP fluorescence intensity in the ipsilateral (Q) and contralateral (R) cortical wall.

Data shown are mean ± SEM (n = 4 brains per group). *p < 0.05 (Student's t test). Scale bar: 135 μm (B–G), 95 μm (I and J), 1,200 μm (K and L), 415 μm (M and N), and 623 μm (O and P).

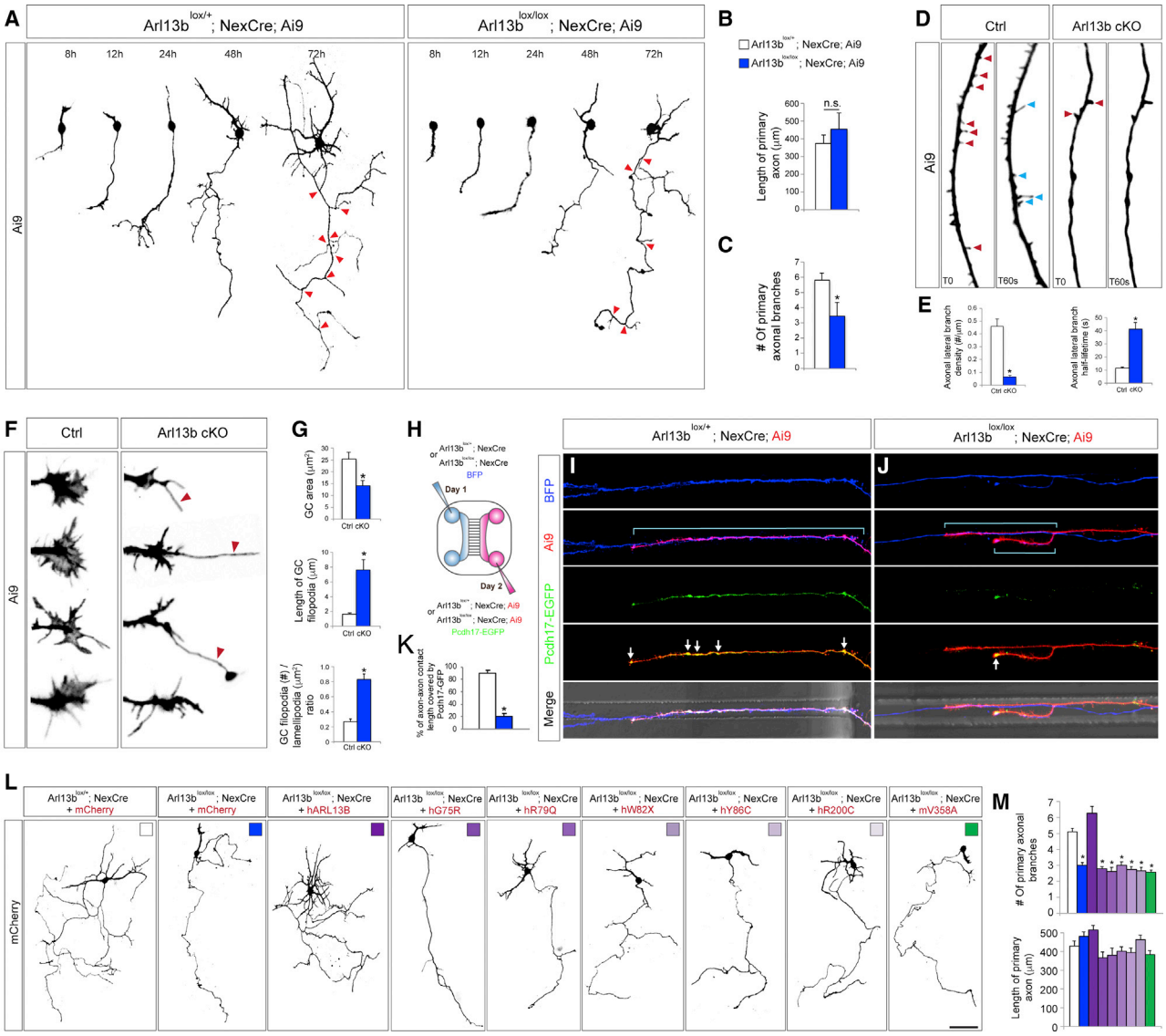

Figure 3. Deletion of *Arl13b* Leads to Axonal Growth Defects *In Vitro*

(A) Growth of DCN neurons dissociated from *Arl13b*$^{lox/+}$*; NexCre*; *Ai9* and *Arl13b*$^{lox/lox}$*; NexCre; Ai9* (cKO) brains (P2) were analyzed at different time points as indicated. Red arrowheads point to the primary axonal branching points.

(B and C) Quantification of axonal outgrowth (length [B] and branches [C]) at 3 days *in vitro* (DIV). Data shown are mean ± SEM (n = 24 neurons). *p < 0.05 (Student's t test).

(D) Axonal filopodia dynamics of DCN neurons from *Arl13b*$^{lox/+}$*; NexCre; Ai9* (Ctrl) and *Arl13b*$^{lox/lox}$*; NexCre; Ai9* (Arl13b cKO) brains. Red arrowheads point to representative axonal filipodia at time 0 s. Blue arrowheads point to newly formed axonal filopodia at time 60 s.

(E) Quantification of axonal lateral branch density and half lifetime. Data shown are mean ± SEM (n = 24 neurons). *p < 0.05 (Student's t test).

(F) Representative axonal growth cones of DCN neurons from Ctrl and Arl13b cKO brains. Red arrowheads point to aberrantly long filopodia extensions.

(G) Quantification of axonal growth cone (GC) area, axonal filopodia length, and growth cone filopodia/lamellipodia ratio. Data shown are mean ± SEM (n = 28 cells). *p < 0.05 (Student's t test).

(H) Schematic of the microfluidic chamber assay for the expression of Pcdh17-EGFP along axon-axon contacts.

(I and J) Expression of Pcdh17-GFP along the BFP$^+$/tdTom$^+$ axon-axon contact sites in DCN neurons of Ctrl (I) and Arl13b cKO (J) brains. White brackets indicate BFP$^+$/tdTom$^+$ axon-axon contact regions. White arrows point to Pcdh17 expression at axon-axon contact sites.

(K) Quantification of Pcdh17-EGFP$^+$ axon-axon contacts.

(L) Effect of human ARL13B mutations on axon growth. DCN neurons of *Arl13b*$^{lox/+}$; *NexCre* and *Arl13b*$^{lox/lox}$*; NexCre* were transfected with mCherry, mCherry-ARL13B (wild type or different human mutations), or mV358A mutant and analyzed after 3 days.

(M) Quantification of primary axonal length and branch number. Data shown are mean ± SEM. *p < 0.05 (one-way ANOVA: $F_{8,216} = 24.11$; p = 4.7E−33; post-hoc $p_{[lox/+\ versus\ lox/lox]}$ = 6.0E−14; post-hoc $p_{[lox/+\ versus\ lox/lox\text{-}ARL13B]}$ = 0.09; post-hoc $p_{[lox/+\ versus\ lox/lox\text{-}G75R]}$ = 5.6E−10; post-hoc $p_{[lox/+\ versus\ lox/lox\text{-}R79Q]}$ = 6.8E−09; post-hoc $p_{[lox/+\ versus\ lox/lox\text{-}W82X]}$ = 9.5E−09; post-hoc $p_{[lox/+\ versus\ lox/lox\text{-}Y86C]}$ = 4.8E−10; post-hoc $p_{[lox/+\ versus\ lox/lox\text{-}R200C]}$ = 2.1E−10; post-hoc $p_{[lox/+\ versus\ lox/lox\text{-}V358A]}$ = 2.5E−11; 25 neurons). Scale bar: 28 μm (A), 8 μm (D and F), 4.5 μm (J and K), and 30 μm (L). See also Figure S5.

BFP (Blue Fluorescent Protein) or tdTomato/Pcdh17-EGFP were plated onto different sides of microfluidic chambers, allowing for the establishment of direct axon-axon contacts between BFP^+ and $tdTom^+$ neurons (Figure 3H). Compared to control neurons that show expression of Pcdh17 at axonal points of contacts, Arl13b-deficient neurons show reduced recruitment of Pcdh17 to axon-axon contacts (Figures 3I–3K). These observations suggest that disrupted ciliary signaling in Arl13b-deficient neurons can impair axon-axon recognition and adhesion signals necessary for the organized growth of axonal tracts.

Multiple mutations (p. R79Q, p. W82X, p. Y86C, p. R200C, and p. G75R) in ARL13B are known to cause JSRD (Cantagrel et al., 2008; Juric-Sekhar et al., 2012; Miertzschke et al., 2014; Parisi, 2019; Rafiullah et al., 2017; Thomas et al., 2015). To test whether these JSRD mutant alleles affect axonal growth, we cre-inducibly expressed them in Arl13b-deficient DCN neurons (Guo et al., 2017). Wild-type human ARL13B rescued the branching defects in the Arl13b-deficient DCN neurons (Figures 3L and 3M). However, JSRD-causing variants R79Q, G75R, W82X, Y86C, and R200C failed to do so consistent with their known disruption of Inpp5e ciliary targeting (Figures 3L and 3M; Humbert et al., 2012). These results suggest that human mutations in Arl13b disrupt axonal development. Further, a mouse non-ciliary form of functional Arl13b (V358A; Higginbotham et al., 2012) also did not rescue the axonal branching defects in Arl13b-deficient DCN neurons (Figures 3L and 3M), suggesting that the localization and activity of Arl13b within the primary cilium is crucial to its role in the appropriate regulation of axonal growth pattern.

Collectively, these observations reveal that neurons deficient in ciliary Arl13b display reduced axonal branching, aberrant growth cone morphology, altered filopodia-lamellipodial balance, and impaired axon-axon adhesive contacts.

Arl13b-Inpp5e Pathway

To define the signaling mechanisms underlying Arl13b-mediated axonal dynamics, we first examined inositol polyphosphate-5-phosphatase (Inpp5e) as Inpp5e is absent in *Arl13b*-deficient cilia indicating Arl13b is necessary for Inpp5e ciliary targeting (Humbert et al., 2012). Inpp5e hydrolyzes the 5-phosphate of PtdIns(4,5)P2 and PtdIns(3,4,5)P3 (PIP2 and PIP3), which act as docking phospholipids necessary for ciliary localization of signaling receptors and activation of signaling cascades. Importantly, mutations in *INPP5E* lead to JSRD and axonal tract defects (Bielas et al., 2009; Conduit et al., 2012; Garcia-Gonzalo et al., 2015; Jacoby et al., 2009). These observations suggest that Inpp5e acts as an effector of Arl13b. The deficiency of ciliary Inpp5e, due to either deletion of *Arl13b* or *Inpp5e*, may compromise the Arl13b-Inpp5e signaling pathway necessary for axonal tract development.

We therefore examined SCP, CST, and CC tract formation and organization in *Inpp5e-NexCre* (Inpp5e cKO) brains. Similar to *Arl13b-NexCre* mutants, *Inpp5e-NexCre* mutant SCP tracts are diffused, wider, and loosely fasciculated (Figures 4A–4D; SCP width [axial]: control, 285 ± 19 μm, Inpp5e cKO, 349 ± 23 μm; $p < 0.05$ (Student's t test); n = 6 brains per group). Mutant CST tract displays reduced pyramidal decussation (Figures 4E–4G). Inpp5e-deficient callosal axons show significantly reduced branching and target innervation when compared to controls (Figures 4H–4M). Further, reduced axonal branching and aberrant growth cone morphology similar to that of Arl13b-deficient neurons were seen Inpp5e-deficient DCN neurons *in vitro* (Figures 4N–4Q). Reduced dendritic growth is also evident in Inpp5e mutant DCN neurons *in vitro* (Figure 4N; total dendritic $length_{[DIV3]}$: control (292.1 ± 23.4 μm), mutant (101.5 ± 8.3 μm), Student's t test, p = 1.28E−13; # of primary $dendrites_{[DIV3]}$: control (5.3 ± 0.6), mutant (2.9 ± 0.2), Student's t test, p = 1.52E−09, n = 16 neurons).

These common defects in Arl13b and Inpp5e-deficient neurons suggest that both can regulate neuronal development from the cilium. We therefore set out to delineate the Arl13b-Inpp5e-regulated signaling mechanisms, which when perturbed in cilia, could affect axonal development.

Arl13b-Inpp5e Pathway Converges on Ciliary-PI3K/AKT Signaling

PI(4,5)P2 and PI(3,4,5)P3, the main substrates of Inpp5e downstream of Arl13b, are major second messengers of receptor tyrosine kinases (RTK), G protein-coupled receptors (GPCRs), and Shh pathways (Bielas et al., 2009; Conduit et al., 2012; Garcia-Gonzalo et al., 2015; Oude Weernink et al., 2007; Phua et al., 2017). Several RTKs, GPCRs, and Smo receptors selectively accumulate in neuronal primary cilia (Christensen et al., 2012; Hilgendorf et al., 2016; Reiter and Leroux, 2017). Upon activation, GPCR, Shh, and RTK signaling lead to the activation of PI3K and the production of PIP3, which in turn activates AKT to orchestrate a broad spectrum of cellular functions, including axonal outgrowth and growth cone dynamics (Hakim et al., 2012; Henle et al., 2011; Manning and Cantley, 2007; Manning and Toker, 2017; Oude Weernink et al., 2007). Consistent with the role of Inpp5e that hydrolyzes PIP3, deletion of Inpp5e leads to enrichment of PIP3 at primary cilia and elevated whole-cell PI3K-AKT signaling activity (Dyson et al., 2017; Phua et al., 2017; Plotnikova et al., 2015). To test the hypothesis that ciliary Arl13b-Inpp5e signaling converges onto the production of ciliary PIP3 and activation of AKT to regulate axonal development, we first examined the level of PIP3 in Arl13b and Inpp5e-deficient neuronal cilia. We expressed PIP3 biosensors $RFP\text{-}PH_{AKT}$ or $mCh\text{-}PH_{GRPI}$ in DCN neurons from control, Arl13b cKO, and Inpp5e cKO brains (Idevall-Hagren et al., 2012). Compared to control, a significant increase in the levels of PIP3 was observed in Arl13b and Inpp5e-deficient neuronal primary cilia (Figures S6A–S6E). We found a similar increase of the PIP3 level in *Arl13b* null cortical neurons (Figures S6F–S6K). These observations suggest that deletion of *Arl13b* or *Inpp5e* leads to increased ciliary PIP3. To test whether the increased PIP3 levels lead to elevated activity of AKT, we examined the phosphorylation level of AKT and its downstream effectors glycogen synthase kinase 3 (GSK3), ribosomal protein S6 kinase (S6K), and transcription factor cyclic AMP-response element binding protein (CREB), in control and Arl13b null or Inpp5e-deficient (*Inpp5e^{rdg}*; Su et al., 2012) brains. A significant increase of p-AKT, p-GSK, p-S6, and p-CREB is evident in both Arl13b- and Inpp5e-deficient brains (Figures S6L and S6M), suggesting an elevated global level of AKT activity follows the loss of Arl13b or Inpp5e. Taken together, these results reveal that the deficiency of Arl13b-Inpp5e in neurons leads to increased levels of ciliary PIP3 as well as elevated global AKT activity.

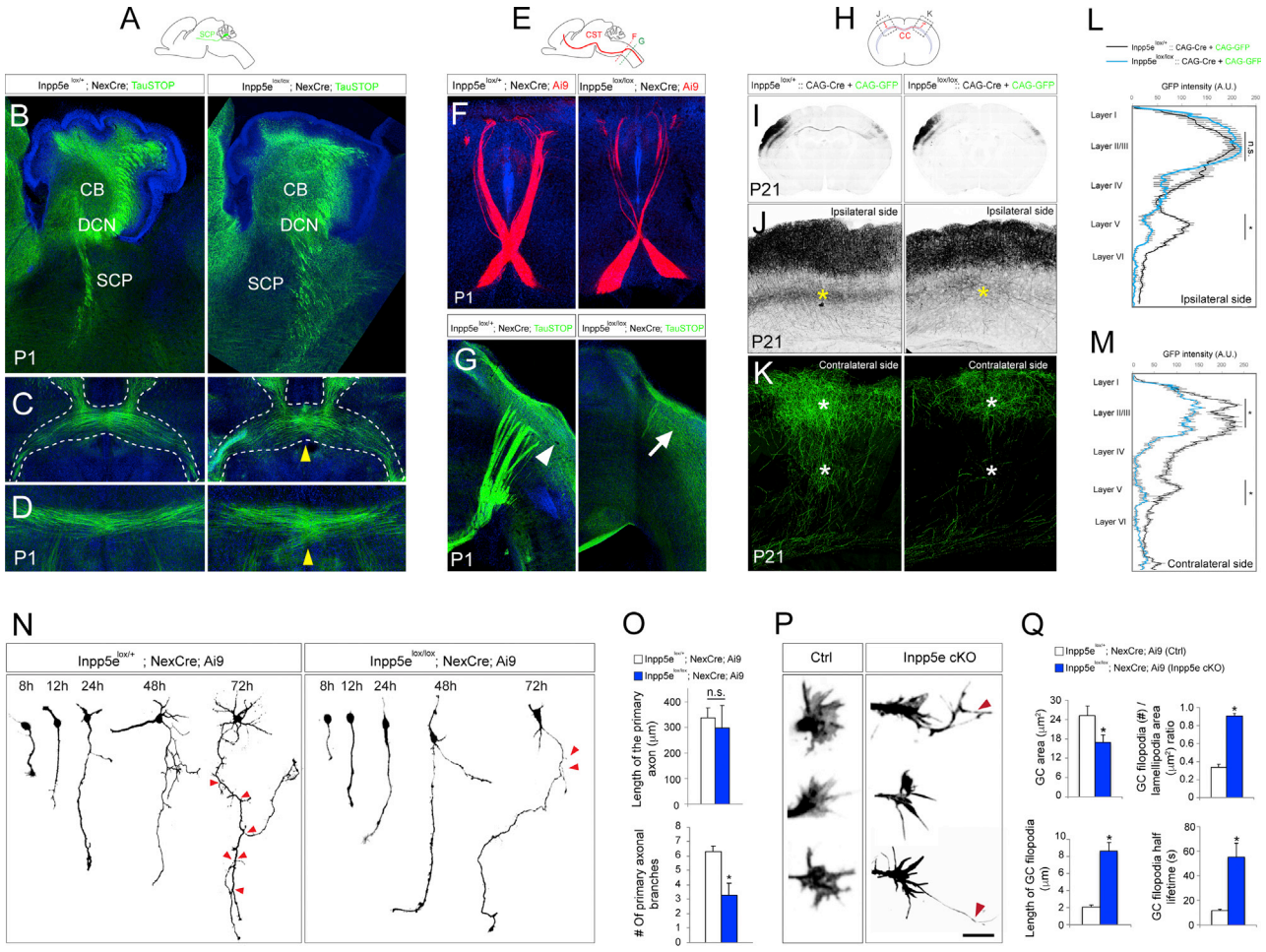

Figure 4. Deletion of *Inpp5e* Leads to Axonal Defects Similar to Arl13b cKO

(A) Schematic of SCP tract in sagittal sections.

(B–D) GFP labeling in *Inpp5e*$^{lox/+}$*; NexCre*; *Taustop* and *Inpp5e*$^{lox/lox}$*; NexCre; Taustop* brains (P1) show the trajectory of SCP tract in sagittal (B), axial (C), and coronal (D) sections. (B) Diffused outgrowth of SCP in Inpp5e cKO when compared to control. Dashed lines (C) outline the SCP decussation in axial sections. Yellow arrowheads in (C) and (D) point to the diffused, wider, and disrupted decussation of SCP in Inpp5e mutants.

(E) Schematic of CST tract in sagittal sections. Dashed lines indicate where (F) and (G) were imaged, respectively.

(F) Altered decussation of TdTom^{+} CST in *Inpp5e*$^{lox/lox}$*; NexCre; Ai9* brains.

(G) Reduced GFP^{+} CST tract fascicles post-decussation and reduced extension of CST axons into the dorsal spinal cord in mutants (arrow; compare to control [arrowhead]).

(H) Schematic of CC tract in coronal sections. Outlined areas indicate where (J) and (K) were imaged.

(I–K) *Inpp5e*$^{lox/+}$ and *Inpp5e*$^{lox/lox}$ embryos (E15) were electroporated with pCAG-Cre and pCAG-GFP plasmids and analyzed at P21. (I) Low-magnification images of GFP labeled CC tract. (J and K) Reduced axonal branching is evident in ipsilateral layer 5 (yellow asterisk) and contralateral layers 2/3 and 5 (white asterisks) in *Inpp5e*$^{lox/lox}$ brains electroporated with pCAG-Cre.

(L and M) Quantification of GFP fluorescence intensity (arbitrary units) along the cortical wall of ipsilateral side (L) and contralateral side (M). Data shown are mean ± SEM (n = 4 brains). *p < 0.05 (Student's t test).

(N) Dissociated DCN neurons from *Inpp5e*$^{lox/+}$*; NexCre; Ai9* (Ctrl) and *Inpp5e*$^{lox/lox}$*; NexCre; Ai9* (Inpp5e cKO) brains were analyzed at different time points as indicated. Red arrowheads point to the primary axonal branching points.

(O) Quantification of axonal outgrowth (3 DIV). Data shown are mean ± SEM (n = 24 neurons). *p < 0.05 (Student's t test).

(P) Representative axonal growth cones of DCN neurons from Ctrl and Inpp5e cKO brains. Red arrowheads point to aberrantly long filopodial extensions.

(Q) Quantification of axonal growth cone area, filopodia length, filopodial half lifetime, and growth cone filopodia/lamellipodia ratio. Data shown are mean ± SEM (n = 24 cells). *p < 0.05 (Student's t test). CB, cerebellum; DCN, deep cerebellar nuclei; SCP, superior cerebellar peduncle; GC, growth cone. Scale bar: 205 μm (B), 150 μm (C and D), 600 μm (F and G), 1,215 μm (I), 240 μm (J), 340 μm (K), 25 μm (N), and 5 μm (P).

Optogenetic and Chemogenetic Manipulations of Ciliary GPCR and Ciliary PI3K/AKT Signaling Change Axonal Behavior

We, therefore, set out to further delineate the role of cilia-regulated PI3K/AKT pathway on axonal development. First, to evaluate the effect of acute activation of ciliary signaling receptors upstream of PI3K on axons, we focused on ciliary GPCR signaling that can activate the PI3K signaling pathway (Figure 5A; Spangler and Bruchas, 2017). We employed a chemogenetic approach using DREADDs (designer receptors exclusively activated by designer

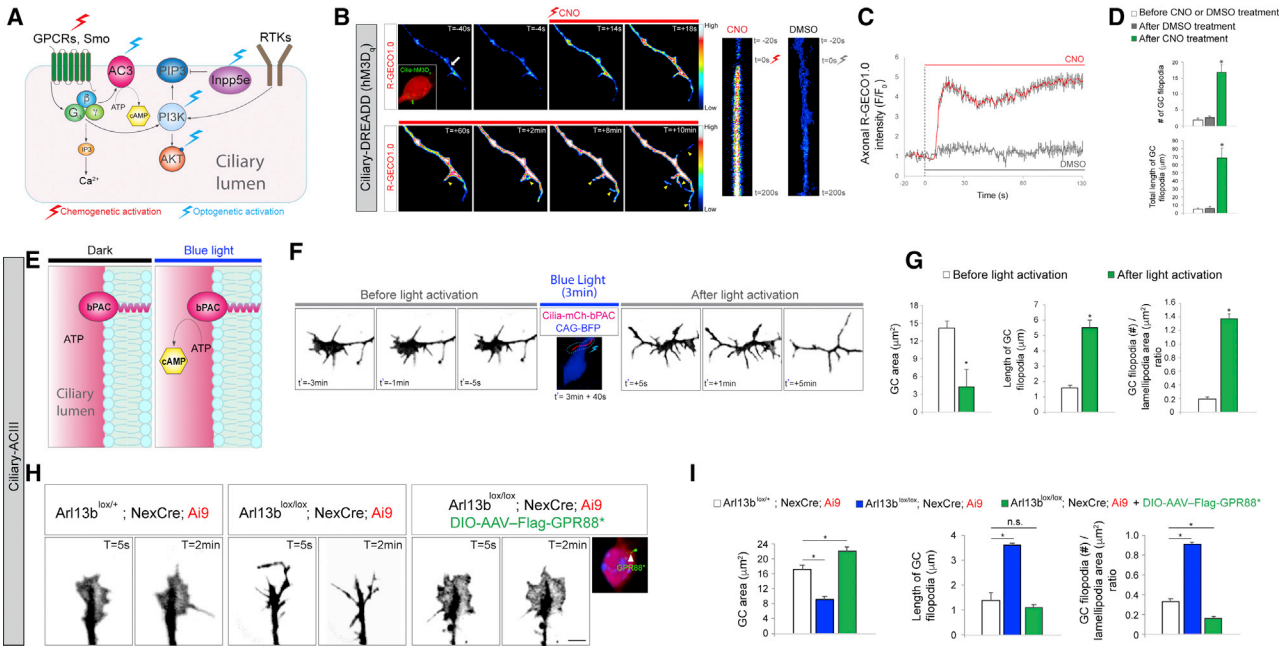

Figure 5. Chemogenetic or Optogenetic Manipulation of Ciliary GPCR Signaling Leads to Rapid Changes in Axonal Growth Cone Dynamics

(A) Schematic depicting optogenetic or chemogenetic approaches to manipulate different interrelated ciliary signaling pathways (GPCRs, ACIII, PI3K, AKT, and Inpp5e).

(B) Time-lapse imaging of control DCN neuron axon expressing Cilia-hM3D$_q$ and RFP-GECO1.0 (pseudocolored) treated with 10μM CNO (left panel). Yellow arrowheads point to the filopodial extensions. Kymograph of the changes in RFP-GECO1.0 fluorescence intensity at the distal axonal tip (white arrow at T0) upon CNO or DMSO treatment.

(C) Axonal RFP-GECO1.0 fluorescence intensity before and after CNO or DMSO treatment (n = 16 cells). Data shown are mean ± SEM. Relative intensity of RFP (F/F_0) at peak [CNO versus DMSO]: p = 1.2E−8, Student's t test.

(D) Quantification of changes in the growth cone morphology before and after CNO or DMSO treatment. Data shown are mean ± SEM (n = 24 neurons). *p < 0.05 (Student's t test).

(E) Schematic of bPAC mediated, blue light-dependent cAMP production in primary cilia.

(F and G) Changes in the growth cone morphology before and after ciliary activation of bPAC in control DCN neurons expressing Cilia-bPAC and pCAG-BFP. t′ in (F) includes 20 s to move from growth cone (pre-light activation) to primary cilia, blue light photo-activation of primary cilia (3 min) and 20 s to move back to growth cone (post-light activation). (G) Quantification of changes in the growth cone morphology before and after light activation. Data shown are mean ± SEM (n = 24 neurons). *p < 0.05 (Student's t test).

(H) Inhibition of ciliary ACIII activity with modified GPR88* in Arl13b-deficient neurons. Live imaging of growth cone dynamics in *Arl13b$^{lox/+}$; NexCre; Ai9*, *Arl13b$^{lox/lox}$; NexCre; Ai9, and Arl13b$^{lox/lox}$; NexCre; Ai9*+ DIO-AAV-Flag-GPR88* DCN neurons. Inset shows expression of FLAG tagged GPR88* in cilium.

(I) Quantification of growth cone (GC) morphology. Data shown are mean ± SEM. *p < 0.05 (one-way ANOVA: $F_{2,42[GC\ area]}$ = 32.0; p = 3.6E−9; post-hoc $p_{[GC\ area,\ lox/+\ versus\ lox/lox]}$ = 6.9E−06; post-hoc $p_{[GC\ area,\ lox/+\ versus\ lox/lox\text{-}GPR88^*]}$ = 0.01; $F_{2,42[\#\ of\ GC\ filopodia]}$ = 36.6; p = 6.2E−10; post-hoc $p_{[\#\ of\ filopodia,\ lox/+\ versus\ lox/lox]}$ = 1.1E−04; post-hoc $p_{[lox/+\ versus\ lox/lox\text{-}GPR88^*]}$ = 0.001; $F_{2,42[L\ of\ GC\ filopodia]}$ = 50.4; p = 6.9E−12; post-hoc $p_{[L\ of\ GC\ filopodia,\ lox/+\ versus\ lox/lox]}$ = 1.8E−07; post-hoc $p_{[L\ of\ GC\ filopodia,\ lox/+\ versus\ lox/lox\text{-}GPR88]}$ = 0.07; n = 15 neurons). Scale bar: 4μm (B) and 8.5 μm (F and H).

drugs) to control GPCR signaling specifically in neuronal cilia (Guo et al., 2017). DREADDs are mutant GPCRs (M3-muscarinic receptors) that have been molecularly evolved to be activated by the small molecule clozapine N-oxide (CNO). Our approach entails cilia-specific expression of a DREADD, hM3D$_q$ that couples to G$_q$ and can induce Ca^{2+} activation when activated by CNO (Armbruster et al., 2007; Dong et al., 2010). Cilia-targeting sequence (CLVCCWFKKSKTRKIKP) (Follit et al., 2010) was used to drive the ciliary localization of hM3D$_q$ (Cilia-hM3D$_q$). We have previously shown that Cilia-hM3D$_q$ triggers cilia-specific GPCR activation and related Ca^{2+} signaling (Guo et al., 2017). The expression of Cilia-hM3D$_q$ did not significantly change the length of primary cilia (Cilia-GFP: 2.72 ± 0.10 μm, Cilia-hM3D$_q$: 2.64 ± 0.11 μm, Student's t test, p = 0.56, n = 14 neurons). Cilia-hM3D$_q$ and Ca^{2+} sensor RFP-GECO1.0 were co-expressed in DCN neurons. Upon 10 μM CNO treatment, filopodial protrusions, correlated with Ca^{2+} elevation ($t_{1/2}$ = 8.34 ± 3.13 s, n = 16 cells), start to emerge at the distal end of axons (Figures 5B–5D). In contrast, control DMSO treatment did not change axonal growth cone dynamics or Ca^{2+} level (Figures 5B–5D). Further, ACIII (adenylate cyclase III), a member of type III adenylate cyclase family that can potently induce cyclic AMP (cAMP), downstream of GPCR signaling activation, is selectively expressed in neuronal primary cilia. Optogenetic activation of a blue light-sensitive, cilia-targeted type III adenylyl cyclase (Cilia-bPAC; (Jansen et al., 2015; Stierl et al., 2011) led to cAMP induction and rapid filopodial protrusions (Figures 5E and 5F) similar to Cilia-hM3D$_q$ activation (Figures 5F and 5G). The expression of Cilia-bPAC did not significantly change the length of primary cilia (Cilia-GFP: 2.62 ± 0.13 μm, Cilia-bPAC: 2.96 ± 0.12 μm, Student's t test, p = 0.51, n = $12_{[Cilia\text{-}GFP]}$, $16_{[Cilia\text{-}bPAC]}$ neurons). In contrast, inhibition of ciliary ACIII activity with a modified, constitutively active, cilia-specific G$_i$-protein-coupled

receptor, GPR88* (Siljee et al., 2018) in Arl13b-deficient neurons leads to opposite effects on filopodia-lamellipodial balance. GPR88* rescued the growth cone and filopodia phenotypes of the Arl13b-deficient neurons, reducing filopodial protrusions and increasing lamellipodial area (Figures 5H and 5I). These results suggest that the activity of ciliary GPCRs can regulate axonal growth cone morphology and dynamics.

To address how the PI3K/AKT signaling, emanating from primary cilia, exerts its impact on axons, we generated optogenetic tools to gain precise, spatiotemporal control of ciliary-PI3K/AKT signaling in neurons and evaluated if selectively activating this signaling pathway in cilia can change axonal behavior (Figure 6A). The blue light activated, CIBN/CRY2 dimerization opto-system was used to selectively recruit PI3-kinase, phosphatidylinositol 5-phosphatase modules (5-Ptase module of Inpp5e), and AKT to cilia membrane (Gradinaru et al., 2010; Idevall-Hagren et al., 2012; Katsura et al., 2015). This optogenetic system is based on blue light (488 nm)-induced dimerization between plant proteins, cryptochrome 2 (CRY2), and the transcription factor CIBN (Idevall-Hagren et al., 2012). CIBN is expressed selectively in cilia using an established ciliary targeting sequence and is anchored to the ciliary plasma membrane through myristoylation (Su et al., 2013). CRY2 is fused to various second messenger modules. Blue light-induced dimerization between CRY2 and the ciliary membrane anchored CIBN (Cilia-CIBN) leads to the recruitment of these modules to cilia. The expression of Cilia-CIBN did not significantly change the length of primary cilia (Cilia-GFP: 2.93 ± 0.22 μm, Cilia-CIBN: 2.89 ± 0.13 μm, Student's t test, $p = 0.82$, $n = 14_{[Cilia-GFP]}$, $15_{[Cilia-CIBN]}$ neurons).

We first examined if activating ciliary-PI3 kinase and generating PIP3 at the ciliary membrane will modulate axonal behavior. To do this, we generated cilia-targeted CIBN (Cilia-CIBN-GFP) and co-expressed it with CRY2-iSH2 in which the inter-SH2 (iSH2) region of the p85α regulatory subunit of class I PI3-kinases is fused with CRY2 in DCN neurons (Idevall-Hagren et al., 2012). iSH2 constitutively binds to the endogenous catalytic p100α-subunit of PI3-kinase and with blue light stimulation the subunits are recruited along with iSH2 domain to the ciliary membrane (Figure 6A). In dark condition, CRY2-iSH2 is mostly enriched at the cytosol (Figure 6B). However, upon a train of 200-ms blue laser (488 nm) illumination solely focused on primary cilium, CRY2-iSH2 is rapidly recruited into the Cilia-CIBN-GFP-expressing cilium ($t_{1/2} = 9 \pm 2.5$ s, $n = 16$ cells) (Figure 6B). Co-expression the PIP3 reporter mCh-PH_{GRPI} with CRY2-iSH2 in these experiments allows simultaneous photo-activation and monitoring of PIP3 production. An increase of PIP3 within cilia was observed ($t_{1/2} = 93 \pm 14$ s, $n = 16$ cells) following ciliary photo-activation (Figure 6C), confirming that ciliary recruitment of PI3 kinase is able to produce PIP3 in the ciliary membrane. We then analyzed the effect of ciliary PI3 kinase activation and PIP3 generation on axonal growth cones. The axonal growth cone dynamics were monitored before and after ciliary PI3 kinase activation in control DCN neurons. Before photo-activation, growth cones display characteristic lamellipodial webbing and short filopodial extensions (Figure 6D). Following blue light activation, growth cones changed their morphology and dynamics (24/29 cells), retracting lamellipodia while extending numerous aberrantly longer filopodial like protrusions, within 30 s of blue light illumination (Figures 6D and 6E). In contrast to the short-lived filopodial protrusions before photo-activation with a half-life time $t_{1/2} = 24 \pm 1.4$s ($n = 24$ cells), the filopodial protrusions formed after photo-activation are highly stable over the imaging duration (20 min). We confirmed that these axonal changes are not due to photo-toxicity induced by the photo-activation, since no changes in PIP3 level or growth cone dynamics were detected upon blue light illumination in neurons expressing only Cilia-GFP/CRY2-iSH2 and no Cilia-CIBN (Figures S7A and S7B). Further, ciliary photo-activation with non-blue light, or blue light illumination at comparably sized, non-ciliary regions in the neuronal soma did not change growth cone dynamics in neurons expressing Cilia-CIBN/CRY2-iSH2 or CIBN/CRY2-iSH2, respectively (Figures S7C–S7F). These results suggest that activation of ciliary PI3 kinase and the resultant production of ciliary PIP3 can rapidly induce changes in neuronal growth cone morphology and dynamics.

PI3-kinase activation and PIP3 production triggers AKT activation. To test if ciliary activation of AKT can induce similar changes in axonal dynamics, the kinase domain of AKT fused with CRY2 (mCh-CRY2-AKT; Katsura et al. 2015) was co-expressed with Cilia-CIBN-GFP in DCN neurons to enable blue light-induced AKT recruitment and activation at the ciliary membrane (Figure 6F). Similar to PI3-kinase activation, mCh-CRY2-AKT showed rapid recruitment within the cilia upon ciliary blue light illumination ($t_{1/2} = 31 \pm 5.4$ s, $n = 16$ cells) (Figure 6G), followed by axonal growth cone changes, including reduced growth cone area and extension of filopodial protrusions (Figures 6H and 6I).

In contrast to the enhancement of ciliary PIP3 production in the above experiments, we also tested the effect of ciliary recruitment of $5ptase_{INPP5E}$ to reduce ciliary PIP3 production (Figure 6J). mCh-CRY2-$5ptase_{INPP5E}$, containing the 5-Ptase catalytic module of Inpp5e necessary to hydrolyze PIP3 and PIP2, fused with CRY2, was co-expressed with Cilia-CIBN-GFP (Figure 6K). Ciliary blue light activation of these neurons induced a reduction of ciliary PIP3 (Figure 6L) ($t_{1/2} = 21 \pm 3.4$ s, $n = 16$ cells), which is followed by retraction of filopodia and expansion of lamellipodia webbing ($n = 24$ cells) (Figures 6M and 6N). Ciliary activation of iSH2, AKT, or Inpp5e did not significantly change cilia length (Cilia length: $iSH2_{[before]} = 2.81 \pm 0.1$ μm, $iSH2_{[after]} = 2.78 \pm 0.1$ μm; $AKT_{[before]} = 2.93 \pm 0.2$ μm, $AKT_{[after]} = 2.85 \pm 0.2$ μm; $Inpp5e_{[before]} = 2.87 \pm 0.3$ μm, $Inpp5e_{[after]} = 2.88 \pm 0.1$ μm; Student's t test, $p > 0.05$, $n = 16$ cells/group). Together, these optogenetic manipulations of the ciliary-PI3K signaling reveal that this pathway has the capacity to rapidly and bi-directionally modulate axonal growth cone dynamics.

What are the signaling mechanisms that enable locally activated, ciliary-PI3K signaling to spread to axons? Recent studies show that AKT activation is sustained by a positive feedback loop mediated by PI3K activation and actin polymerization (Katsura et al., 2015). Feedback networks involving kinase-dependent cascades (e.g., PI3K and MAPK signaling) are known to self-perpetuate and rapidly spread local signaling over long distances along the plasma membrane to reach distant cellular targets (Fivaz et al., 2008; Katsura et al., 2015; Kholodenko, 2006; Sawano et al., 2002; Welf et al., 2012). To monitor the axonal changes in PIP3, post-ciliary-PI3 kinase activation, axonal PIP3 reporters (RFP-PH_{AKT} or mCh-PH_{GRPI}) were imaged before and after ciliary activation of PI3-kinase. Both RFP-PH_{AKT} and mCh-PH_{GRPI} showed a gradual increase in the growth cones

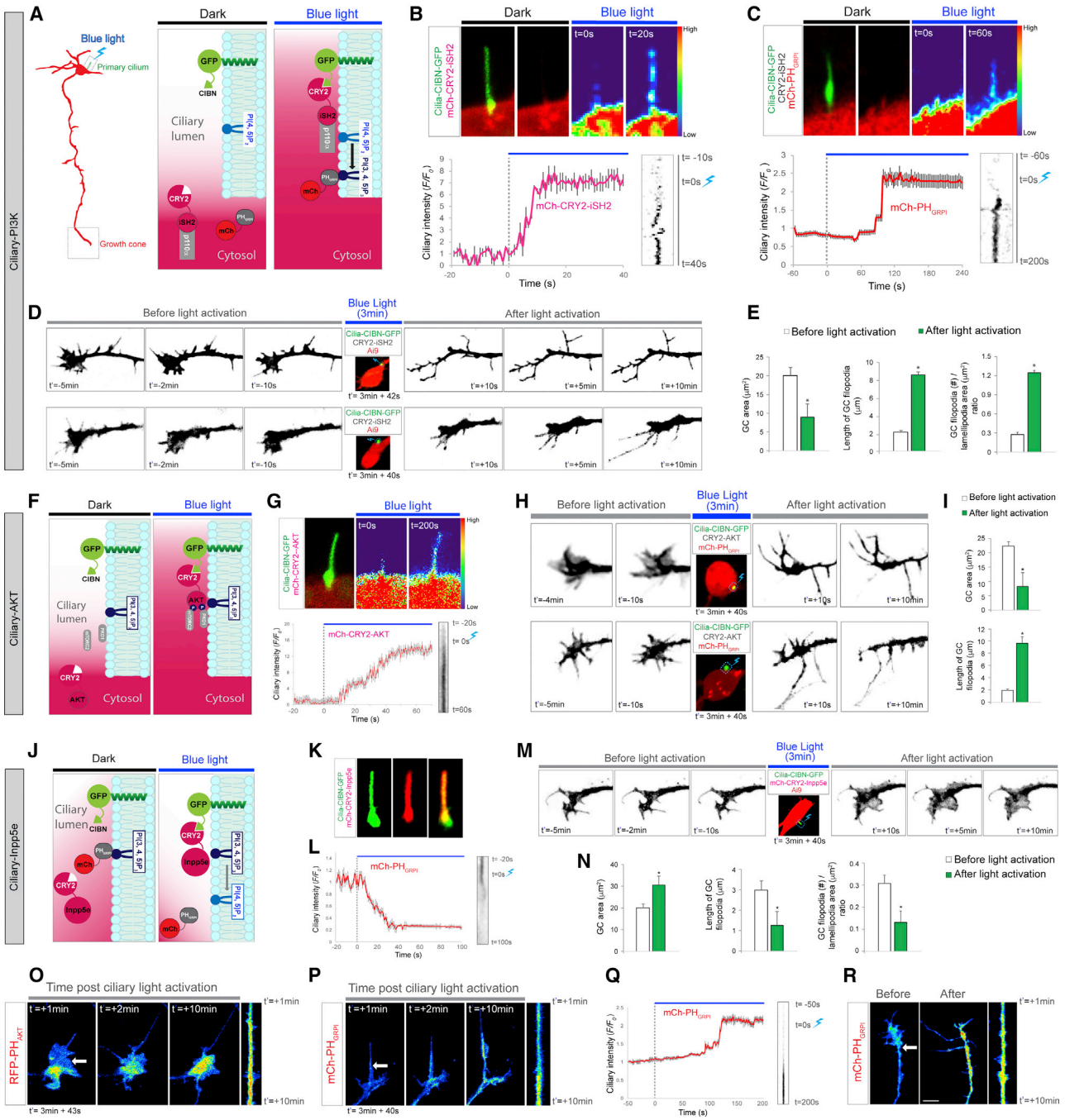

Figure 6. Optogenetic Manipulation of Ciliary PI3K/AKT Signaling Leads to Rapid Changes in Axonal Growth Cone Dynamics

(A) Schematic of optogenetic recruitment of PI3-kinase to the cilium and evaluation of changes in axonal growth cone. Untagged (CRY2-iSH2) or mCherry-tagged iSH2 (mCh-CRY2-iSH2) was used. PIP3 sensor mCh-PH$_{GRPI}$ was not included in experiments where mCh-CRY2-iSH2 was used.

(B and C) Expression of Cilia-CIBN-GFP and mCh-CRY2-iSH2 (B) or mCh-PH$_{GRPI}$ (C) in the primary cilia of control DCN neurons before and after ciliary blue light activation (upper panels, B and C). Lower panels (B and C) illustrate the dynamics and kymographs of the ciliary mCh-CRY2-iSH2 (B) and mCh-PH$_{GRPI}$ (C) intensity before and after ciliary blue light illumination (n = 16 cells).

(D and E) Changes in the growth cone morphology before and after ciliary recruitment of PI3-kinase in two different DCN neurons expressing Cilia-CIBN-GFP and CRY2-iSH2 (D). Quantification of changes in the growth cone morphology before and after light activation (E). Data shown are mean ± SEM (n = 24 neurons). *p < 0.05 (Student's t test).

(F) Schematic of optogenetic recruitment of AKT to the ciliary membrane.

(G) Expression of Cilia-CIBN-GFP and mCh-CRY2-AKT in the primary cilia of control DCN neurons before and after ciliary blue light activation (upper panels). Lower panels illustrate the dynamics and kymograph of ciliary mCh-CRY2-AKT intensity before and after ciliary blue light activation (n = 16 cells).

(legend continued on next page)

post-activation, indicating lateral propagation of PI3K signaling (Figures 6O and 6P). Further, we noticed the ciliary activation of AKT is followed by a gradual increase of PIP3 in primary cilia and growth cones (Figures 6Q and 6R). These data demonstrate that activated PI3K-AKT signaling in cilia can spread signals to axonal growth cones. Consistent with a role for positive feedback loops mediated by PI3K activation and actin polymerization in the propagation of such signaling, inhibition of actin polymerization with low dosage of Latrunculin B known to block AKT-PI3K feedback loop or inhibition of PI3-kinase activity with LY294002 abolished the increase of PIP3 at the growth cone and growth cone morphological changes induced by ciliary PI3K/AKT activation (Figures S7G and S7H).

Ciliary Signaling Regulates Transcriptional Landscape during Axonal Development

In addition to inducing rapid, local changes on axonal behavior, ciliary signaling may also impact transcriptional programs necessary for axonal development (Green and Mykytyn, 2014; McIntyre et al., 2012; Mukhopadhyay and Rohatgi, 2014; Wang et al., 2015). To gain further insights into the cilia signaling regulated transcriptional landscape during neuronal growth and connectivity, we performed RNA-seq analysis of cortices dissected from E12.5 *Arl13b*$^{-/-}$ and littermate control embryos. This analysis identified 135 differentially expressed genes, 130 upregulated and 5 downregulated, in *Arl13b*$^{-/-}$ (Figure S8A). Gene Ontology (GO) analysis suggest that Arl13b deficiency leads to changes in the transcriptional landscape that converge onto biological processes including neural development and differentiation, cell adhesion, cytoskeleton organization, signal transduction, and metabolism (Figure S8B). Moreover, in support of our observation that PI3K/AKT signaling is a central driver of cilia signaling-mediated changes in axonal development, IPA (Ingenuity pathway analysis) gene-gene interaction network analyses suggest that AKT is at the hub, inter-linking differentially expressed genes in Arl13b mutants (Figure S8C). This analysis of global transcriptional changes following *Arl13b* deletion further suggests a role for aberrantly activated PI3K/AKT and related signaling in the manifestation of axonal developmental changes in cilia mutants.

DISCUSSION

Axonal tract defects are a common feature in many human ciliopathies, with JSRD exhibiting the most consistent and distinct axonal malformations such as MTS and abnormal CST organization. Here, using two, projection neuron-specific JSRD mouse models and cilia-specific optogenetic and chemogenetic signaling approaches, we demonstrate that primary cilia-driven signaling regulates proper growth cone dynamics and axonal development. Collectively, these results indicate that ciliary receptor activation and the resultant changes in convergent signaling cascades (e.g., PI3K, AKT, and AC3) can effectively modulate of axonal behavior. These studies reveal a new cellular mechanism vital for the formation of neuronal connectivity in the mammalian brain and provide new insights into JSRD pathology.

Axonal Defects Related to JSRD

During the formation of the connectome in the brain, axons are guided by tropic and trophic gradients of chemoattractant or chemorepellent cues toward their target. Axons travel in large tracts or fascicles and follow stereotyped pathways to reach synaptic targets. Group extension of axons toward appropriate targets is necessary for neuronal wiring in the brain (Fame et al., 2011). Our observations show that while the axonogenesis or extension of axons are not affected in cilia mutants, the branching, fasciculation, crossing of axons and thus their accurate final projections are disrupted in cilia mutants.

Both a motile growth cone at the tip of the extending axon that properly responds to guidance cues and axon branching that enables axon sorting and fasciculation are crucial to ensure the fidelity of axonal tract development (Cioni et al., 2018; Nishikimi et al., 2013; Raper and Mason, 2010; Wang and Marquardt, 2013; Yu and Bargmann, 2001). Growth cone motility relies on the interplay between filopodia that sense environmental cues for pathfinding and lamellipodia that support persistent axonal outgrowth (Mattila and Lappalainen, 2008; Mejillano et al., 2004; Vitriol and Zheng, 2012). Filopodia are necessary to initiate axon branches (Dent et al., 2004; Winkle et al., 2016). Branching along the axonal shafts enable projecting axons to connect with additional targets en route. Once reaching their appropriate final target, axons establish connections by extending terminal axon arbors (Gibson and Ma, 2011; Kalil and Dent, 2014). We found that cilia mutant neurons show altered filopodia versus lamellipodia balance and disrupted branching. Arl13b or Inpp5e-deficient neurons grow a long primary axon with significantly reduced lateral axonal branches and terminal arbors at targets, thus failing to sufficiently innervate their targets to form appropriate neuronal connections. These observations suggest that disruption of primary cilia-mediated modulation of axonal growth cone and branching dynamics contributes to the axon-axon

(H and I) Changes in the growth cone morphology before and after ciliary recruitment of AKT in two different DCN neurons expressing Cilia-CIBN-GFP, CRY2-AKT, and mCh-PH_{GRPI} (H). Quantification of changes in the growth cone morphology before and after light activation (I). Data shown are mean ± SEM (n = 24 neurons). *p < 0.05 (Student's t test).

(J) Schematic of optogenetic recruitment of $5pase_{INPP5E}$ to the ciliary membrane.

(K) Expression of Cilia-CIBN-GFP and mCh-CRY2-$5pase_{INPP5E}$ in the primary cilia of DCN neurons.

(L) Dynamics and kymograph of PIP3 sensor mCh-PH_{GRPI} intensity in primary cilia after ciliary recruitment of $5pase_{INPP5E}$ (n = 16 cells).

(M and N) Changes in the growth cone morphology before and after ciliary recruitment of $5pase_{INPP5E}$ in DCN neurons expressing Cilia-CIBN-GFP and mCh-CRY2-$5pase_{INPP5E}$ (M). Quantification of changes in the growth cone morphology before and after light activation (N). Data shown are mean ± SEM (n = 24 neurons). *p < 0.05 (Student's t test).

(O and P) Changes in fluorescence intensity of PIP3 reporters, RFP-PH_{AKT} (O) and mCh-PH_{GRPI} (P), in axonal growth cone (white arrow) after ciliary activation of PI3-kinase.

(Q and R) Dynamics and kymograph of mCh-PH_{GRPI} intensity in primary cilia (Q) and axonal growth cone (R) after ciliary activation of AKT (n = 16 cells). t′ in (D), (H), (M), (O), (P), and (R) includes 20 s to move from growth cone (pre-light activation) to primary cilia, blue light photo-activation of primary cilia (3 min) and 20–23 s to move back to growth cone (post-light activation). Scale bar: 1.5 μm (B, C, G, K, O, P, and R); 2.5 μm (D, H, and M). See also Figure S7.

interaction and axonal pathfinding defects in cilia mutants. However, the nature of ciliary modulation of axonal response to guidance cues such as Netrin, Slit, Semaphorin, Ephrin, and Wnt during axonal pathfinding remains to be fully elucidated.

Patients with every ARL13B and INPP5E mutation suffer from intellectual disabilities and psychomotor delay. ARL13B^{G75R} mutant patients also suffer from epilepsy. While these neurological phenotypes clearly suggest circuit malfunction, apart from major axonal pathway defects detectable in MRI, other deficits such as neuronal dendritic disruptions are yet to be defined in genotyped JSRD patient brain tissue. Future studies focused on examining how these disease-causing mutations affect the interactions between ARL1B and INPP5E as well as the interactome of ARL13B would be essential to further dissect the Arl13b-Inpp5e-driven signaling mechanisms underlying JSRD.

Primary Cilium as a Signaling Node during Axonal Development

Primary cilium, with a volume ~ 1/1,000 of the soma, possesses diverse signaling machineries, including RTKs (e.g., IGFR, EGFR, PDGFR-α, Trk receptors p75^{NTR}, and TrkB) and GPCRs (e.g., Smo, Frizzled receptor FZD3, Sstr3, 5HT6, NPY2R, NPY5R, D2, MchR1, and GPR161), their downstream effectors (e.g., PI3 kinase, Inpp5b, Inpp5e, Ocrl, AKT, CaMKIIβ, AC3, AC5, and AC6), and second messengers (e.g., PIP3, PIP2, Ca^{2+}, and cAMP), thus, providing a unique environment where signaling components are highly concentrated in a small cellular domain to facilitate efficient signaling activation and crosstalk (Arellano et al., 2012; Armato et al., 2011; Choi et al., 2011; Christensen et al., 2012; Conduit et al., 2012; DeCaen et al., 2013; Delling et al., 2013; Franco et al., 2014; Green and Mykytyn, 2014; Guo et al., 2015; Hilgendorf et al., 2016; Jacoby et al., 2009; Mukhopadhyay and Rohatgi, 2014; Nichols et al., 2013; Omori et al., 2015; Phua et al., 2015; Puram et al., 2011; Schou et al., 2015; Zhu et al., 2009). However, due to the lack of methods to exert precise control of cilia-specific signaling events, the exact cellular and physiological impact of the signaling emanating from primary cilia on the developing neurons and neural circuit formation remained poorly understood. To overcome this limitation, we employed a combination of mouse genetics, chemogenetic, and optogenetic approaches to enable the interrogation of ciliary signaling in the developing neurons. Collectively, our observations suggest that altered ciliary PI3K/AKT signaling homeostasis underlies the aberrant axonal growth cone dynamics in cilia mutant neurons and that signals emanating from cilia have the capacity to remotely regulate axonal growth cone behavior changes over long distance, via a yet-to-be defined modes of propagation.

Propagation of Ciliary Signaling in Neurons

Deficiency of Inpp5e, the main inositol polyphosphate-5-phosphatase within cilia, disrupts the ciliary membrane phosphoinositide (PIP/PIP2/PIP3) composition and results in dysregulation of Shh and PI3K/AKT signaling (Chávez et al., 2015; Conduit et al., 2012; Dyson et al., 2017; Eramo and Mitchell, 2016; Garcia-Gonzalo et al., 2015). Our observations show that Inpp5e deficiency caused by *Arl13b* or *Inpp5e* deletion leads to globally elevated PIP3 level and PI3K/AKT activity in developing neurons, supporting the notion that dysregulated ciliary signaling can propagate throughout the whole neuronal cell body to manifest pathogenic changes in normal state.

Once activated, PI3K/AKT signaling employs downstream kinase cascades and second messengers (e.g., Ca^{2+}, cAMP, IP3, and PIP3) to amplify and propagate signals for cell-wide, long-distance signaling (Civelli, 2012; Fruman et al., 2017; Gavi et al., 2006; Lemmon and Schlessinger, 2010). We show that ciliary GPCR signaling induces axonal Ca^{2+} wave down to the growth cone. Previous studies suggest that Shh-Smo signaling, possibly via primary cilia, acts to downregulate cAMP levels and protein kinase A activity in commissural neurons to allow Sema3-mediated repulsion of axons at midline crossing (Parra and Zou, 2010). The exact mechanisms that enable ciliary signaling to trigger axonal Ca^{2+} wave and its integration with axonal PI3K/AKT signaling waves are yet to be fully elucidated. Nevertheless, our observations indicate that ciliary signaling can engage multiple convergent pathways to enable signal propagation across the neuronal cell body.

Primary cilia signaling is likely to influence neuronal behavior via both rapid local signaling cascade changes as well as by triggering changes in transcriptional programs underlying neuronal growth and connectivity. Considering the time window it takes for long projecting axons to grow, navigate, and connect with their distant targets (i.e., several days), primary-cilia-signaling-driven local changes may facilitate rapid fine-tuning of axonal behavior, whereas transcriptional program changes may facilitate permissive conditions for axon growth, navigation, and target recognition. PI3/AKT signaling, in addition to locally changing axonal behavior, is also known to directly regulate transcriptional networks important for axonal development (Chen et al., 2014; Graef et al., 2003; Kwon et al., 2006; Nguyen and Di Giovanni, 2008; Manning and Toker, 2017; Sánchez-Alegría et al., 2018). It is thus conceivable that PI3K/AKT signaling serves as a converging node to integrate ciliary receptor signaling necessary for both rapid axonal tract growth modulation and long-term neuronal developmental program regulation.

This study points to the tantalizing possibility that neuronal primary cilia may customize a "ciliary signaling signature" that elicits cilia-specific impact on neuronal events such as calcium waves, cytoskeletal rearrangements, adhesion, and transcriptional regulation necessary for proper axonal tract development and wiring. In spite of not being required for extension of axons, cilia appear to exert a crucial modulatory role in appropriate axonal wiring. Cilia signaling, from locales where the neuronal soma are, may enable fine-tuning of projection neuron axonal behavior, long distances away, necessary to establish the final axonal connectivity. Cilia may thus serve as modulators that enable coordination of signaling between neuronal origin and target (e.g., DCN and thalamus or cortical projection neuron, and spinal cord) necessary to establish precise patterns of connectivity. Consistent with this, our observations show that neuronal cilia regulate axonal growth cones, at the tip of axonal projections, whose functions are necessary for precise wiring of the neural circuitry. Future efforts to decipher the communication networks between neuronal cilia and their cellular environment or between axons and cilia, in the context of brain development, will facilitate a holistic view of how primary cilia receive and convey environmental signals to modulate brain formation and

organization. Nevertheless, our studies delineate the significance of cilia-driven signaling in axonal tract development and connectivity in the developing brain, thus, defining a hitherto undefined cell biological mechanism fundamental for neuronal circuit formation in the brain and whose dysregulation may underlie axonal tract defects in JSRD.

STAR★METHODS

Detailed methods are provided in the online version of this paper and include the following:

- KEY RESOURCES TABLE
- LEAD CONTACT AND MATERIALS AVAILABILITY
- EXPERIMENTAL MODEL AND METHOD DETAILS
  - Mice
  - DNA Constructs
  - CLARITY Imaging
  - Microfluidic Chamber Assay
  - *In Utero* Electroporation
  - Primary Neuronal Culture and Transfection
  - Chemogenetic Manipulation of Ciliary Signaling and Axonal Imaging
  - Optogenetic Manipulation of Ciliary-PI3K/AKT, Ciliary-Adenylyl Cyclase Signaling, and Axonal Imaging
  - Immunohistochemistry
  - Tissue Culture and Transfection
  - Immunoblotting
  - RNA-Seq
  - Image Analysis
  - RNA-Seq Data Analysis
- QUANTIFICATION AND STATISTICAL ANALYSIS
  - General Statistical Analysis
- DATA AND CODE AVAILABILITY

SUPPLEMENTAL INFORMATION

Supplemental Information can be found online at https://doi.org/10.1016/j.devcel.2019.11.005.

ACKNOWLEDGMENTS

This research was supported by NIH grant NS090029 to E.A. and T.C., Natural Sciences and Engineering Research Council of Canada grant RGPIN-2019-04820 to J.G., F31 NS101806 and T32GM008490 to S.K.S., and the confocal imaging and bioinfomatics cores of NINDS grant 5P30NS045892. We thank A. Kolodkin and A.S. LaMantia for helpful comments.

AUTHOR CONTRIBUTIONS

J.G., T.C., and E.S.A. designed the experiments and supervised the project. J.G., J.O., C.C., L.X., D.W., S.K.S., S.G., S.C., A.L., J.L., K.H.B., T.P., J.M.S., G.D.S., T.C., and E.S.A. conducted the experiments and analyzed the data. J.G., D.W., G.D.S., S.G., T.C., and E.S.A. wrote the manuscript.

DECLARATION OF INTERESTS

The authors declare no competing interests.

Received: March 7, 2019
Revised: August 8, 2019
Accepted: November 10, 2019
Published: December 16, 2019

REFERENCES

Arellano, J.I., Guadiana, S.M., Breunig, J.J., Rakic, P., and Sarkisian, M.R. (2012). Development and distribution of neuronal cilia in mouse neocortex. J. Comp. Neurol. *520*, 848–873.

Armato, U., Chakravarthy, B., Chiarini, A., Prà, I.D., and Whitfield, J.F. (2011). A Paradigm-changing surprise from dentate gyrus granule cells—cilium-localized p75NTR may drive their progenitor cell proliferation. J. Alzheimers Dis. *01*, 1–3.

Armbruster, B.N., Li, X., Pausch, M.H., Herlitze, S., and Roth, B.L. (2007). Evolving the lock to fit the key to create a family of G protein-coupled receptors potently activated by an inert ligand. Proc. Natl. Acad. Sci. USA *104*, 5163–5168.

Banker, G. (2018). The development of neuronal polarity: a retrospective view. J. Neurosci. *38*, 1867–1873.

Barral, D.C., Garg, S., Casalou, C., Watts, G.F.M., Sandoval, J.L., Ramalho, J.S., Hsu, V.W., and Brenner, M.B. (2012). Arl13b regulates endocytic recycling traffic. Proc. Natl. Acad. Sci. USA *109*, 21354–21359.

Bielas, S.L., Silhavy, J.L., Brancati, F., Kisseleva, M.V., Al-Gazali, L., Sztriha, L., Bayoumi, R.A., Zaki, M.S., Abdel-Aleem, A., Rosti, R.O., et al. (2009). Mutations in INPP5E, encoding inositol polyphosphate-5-phosphatase E, link phosphatidyl inositol signaling to the ciliopathies. Nat. Genet. *41*, 1032–1036.

Brancati, F., Dallapiccola, B., and Valente, E.M. (2010). Joubert syndrome and related disorders. Orphanet J. Rare Dis. *5*, 20.

Cantagrel, V., Silhavy, J.L., Bielas, S.L., Swistun, D., Marsh, S.E., Bertrand, J.Y., Audollent, S., Attié-Bitach, T., Holden, K.R., Dobyns, W.B., et al. (2008). Mutations in the cilia gene ARL13B lead to the classical form of Joubert syndrome. Am. J. Hum. Genet. *83*, 170–179.

Caspary, T., Larkins, C.E., and Anderson, K.V. (2007). The graded response to sonic hedgehog depends on cilia architecture. Dev. Cell *12*, 767–778.

Chávez, M., Ena, S., Van Sande, J., de Kerchove d'Exaerde, A., Schurmans, S., and Schiffmann, S.N. (2015). Modulation of ciliary phosphoinositide content regulates trafficking and sonic hedgehog signaling output. Dev. Cell *34*, 338–350.

Chédotal, A., and Richards, L.J. (2010). Wiring the brain: the biology of neuronal guidance. Cold Spring Harbor Perspect. Biol. *2*, a001917.

Chen, J., Alberts, I., and Li, X. (2014). Dysregulation of the IGF-I/PI3K/AKT/mTOR signaling pathway in autism spectrum disorders. Int. J. Dev. Neurosci. *35*, 35–41.

Choi, Y.H., Suzuki, A., Hajarnis, S., Ma, Z., Chapin, H.C., Caplan, M.J., Pontoglio, M., Somlo, S., and Igarashi, P. (2011). Polycystin-2 and phosphodiesterase 4C are components of a ciliary A-kinase anchoring protein complex that is disrupted in cystic kidney diseases. Proc. Natl. Acad. Sci. USA *108*, 10679–10684.

Christensen, S.T., Clement, C.A., Satir, P., and Pedersen, L.B. (2012). Primary cilia and coordination of receptor tyrosine kinase (RTK) signalling. J. Pathol. *226*, 172–184.

Cioni, J.M., Wong, H.H.-W., Bressan, D., Kodama, L., Harris, W.A., and Holt, C.E. (2018). Axon-axon interactions regulate topographic optic tract sorting via CYFIP2-dependent WAVE complex function. Neuron *97*, 1078–1093.e6.

Civelli, O. (2012). Orphan GPCRs and neuromodulation. Neuron *76*, 12–21.

Conduit, S.E., Dyson, J.M., and Mitchell, C.A. (2012). Inositol polyphosphate 5-phosphatases; new players in the regulation of cilia and ciliopathies. FEBS Lett. *586*, 2846–2857.

DeCaen, P.G., Delling, M., Vien, T.N., and Clapham, D.E. (2013). Direct recording and molecular identification of the calcium channel of primary cilia. Nature *504*, 315–318.

Delling, M., DeCaen, P.G., Doerner, J.F., Febvay, S., and Clapham, D.E. (2013). Primary cilia are specialized calcium signalling organelles. Nature *504*, 311–314.

Dent, E.W., Barnes, A.M., Tang, F., and Kalil, K. (2004). Netrin-1 and semaphorin 3A promote or inhibit cortical axon branching, respectively, by reorganization of the cytoskeleton. J. Neurosci. *24*, 3002–3012.

Dong, S., Allen, J.A., Farrell, M., and Roth, B.L. (2010). A chemical-genetic approach for precise spatio-temporal control of cellular signaling. Mol. Biosyst. *6*, 1376–1380.

Dyson, J.M., Conduit, S.E., Feeney, S.J., Hakim, S., DiTommaso, T., Fulcher, A.J., Sriratana, A., Ramm, G., Horan, K.A., Gurung, R., et al. (2017). INPP5E regulates phosphoinositide-dependent cilia transition zone function. J. Cell Biol. *216*, 247–263.

Engle, E.C. (2010). Human genetic disorders of axon guidance. Cold Spring Harbor Perspect. Biol. *2*, a001784.

Eramo, M.J., and Mitchell, C.A. (2016). Regulation of PtdIns(3,4,5)P3/Akt signalling by inositol polyphosphate 5-phosphatases. Biochem. Soc. Trans. *44*, 240–252.

Fame, R.M., MacDonald, J.L., and Macklis, J.D. (2011). Development, specification, and diversity of callosal projection neurons. Trends Neurosci. *34*, 41–50.

Fivaz, M., Bandara, S., Inoue, T., and Meyer, T. (2008). Robust neuronal symmetry breaking by Ras-triggered local positive feedback. Curr. Biol. *18*, 44–50.

Follit, J.A., Li, L., Vucica, Y., and Pazour, G.J. (2010). The cytoplasmic tail of fibrocystin contains a ciliary targeting sequence. J. Cell Biol. *188*, 21–28.

Franco, I., Gulluni, F., Campa, C.C., Costa, C., Margaria, J.P., Ciraolo, E., Martini, M., Monteyne, D., De Luca, E., Germena, G., et al. (2014). PI3K class II alpha controls spatially restricted endosomal PtdIns3P and Rab11 activation to promote primary cilium function. Dev. Cell *28*, 647–658.

Fruman, D.A., Chiu, H., Hopkins, B.D., Bagrodia, S., Cantley, L.C., and Abraham, R.T. (2017). The PI3K pathway in human disease. Cell *170*, 605–635.

Garcia-Gonzalo, F.R., Phua, S.C., Roberson, E.C., Garcia, G., 3rd, Abedin, M., Schurmans, S., Inoue, T., and Reiter, J.F. (2015). Phosphoinositides regulate ciliary protein trafficking to modulate hedgehog signaling. Dev. Cell *34*, 400–409.

Gavi, S., Shumay, E., Wang, H.Y., and Malbon, C.C. (2006). G-protein-coupled receptors and tyrosine kinases: crossroads in cell signaling and regulation. Trends Endocrinol. Metab. *17*, 48–54.

Gibson, D.A., and Ma, L. (2011). Developmental regulation of axon branching in the vertebrate nervous system. Development *138*, 183–195.

Goebbels, S., Bormuth, I., Bode, U., Hermanson, O., Schwab, M.H., and Nave, K.A. (2006). Genetic targeting of principal neurons in neocortex and hippocampus of NEX-Cre mice. Genesis *44*, 611–621.

Gradinaru, V., Zhang, F., Ramakrishnan, C., Mattis, J., Prakash, R., Diester, I., Goshen, I., Thompson, K.R., and Deisseroth, K. (2010). Molecular and cellular approaches for diversifying and extending optogenetics. Cell *141*, 154–165.

Graef, I.A., Wang, F., Charron, F., Chen, L., Neilson, J., Tessier-Lavigne, M., and Crabtree, G.R. (2003). Neurotrophins and netrins require calcineurin/NFAT signaling to stimulate outgrowth of embryonic axons. Cell *113*, 657–670.

Green, J.A., and Mykytyn, K. (2014). Neuronal primary cilia: an underappreciated signaling and sensory organelle in the brain. Neuropsychopharmacology *39*, 244–245.

Green, W.W., Uytingco, C.R., Ukhanov, K., Kolb, Z., Moretta, J., McIntyre, J.C., and Martens, J.R. (2018). Peripheral gene therapeutic rescue of an olfactory Ciliopathy restores sensory input, axonal pathfinding, and odor-guided behavior. J. Neurosci. *38*, 7462–7475.

Guadiana, S.M., Semple-Rowland, S., Daroszewski, D., Madorsky, I., Breunig, J.J., Mykytyn, K., and Sarkisian, M.R. (2013). Arborization of dendrites by developing neocortical neurons is dependent on primary cilia and type 3 adenylyl cyclase. J. Neurosci. *33*, 2626–2638.

Guemez-Gamboa, A., Coufal, N.G., and Gleeson, J.G. (2014). Primary cilia in the developing and mature brain. Neuron *82*, 511–521.

Guo, J., Higginbotham, H., Li, J., Nichols, J., Hirt, J., Ghukasyan, V., and Anton, E.S. (2015). Developmental disruptions underlying brain abnormalities in ciliopathies. Nat. Commun. *6*, 7857.

Guo, J., Otis, J.M., Higginbotham, H., Monckton, C., Cheng, J., Asokan, A., Mykytyn, K., Caspary, T., Stuber, G.D., and Anton, E.S. (2017). Primary cilia signaling shapes the development of interneuronal connectivity. Dev. Cell *42*, 286–300.e4.

Hakim, S., Bertucci, M.C., Conduit, S.E., Vuong, D.L., and Mitchell, C.A. (2012). Inositol polyphosphate phosphatases in human disease. Curr. Top. Microbiol. Immunol. *362*, 247–314.

Hayashi, S., Inoue, Y., Kiyonari, H., Abe, T., Misaki, K., Moriguchi, H., Tanaka, Y., and Takeichi, M. (2014). Protocadherin-17 mediates collective axon extension by recruiting actin regulator complexes to interaxonal contacts. Dev. Cell *30*, 673–687.

Haycraft, C.J., Zhang, Q., Song, B., Jackson, W.S., Detloff, P.J., Serra, R., and Yoder, B.K. (2007). Intraflagellar transport is essential for endochondral bone formation. Development *134*, 307–316.

Henle, S.J., Wang, G., Liang, E., Wu, M., Poo, M.M., and Henley, J.R. (2011). Asymmetric PI(3,4,5)P3 and Akt signaling mediates chemotaxis of axonal growth cones. J. Neurosci. *31*, 7016–7027.

Higginbotham, H., Eom, T.Y., Mariani, L.E., Bachleda, A., Hirt, J., Gukassyan, V., Cusack, C.L., Lai, C., Caspary, T., and Anton, E.S. (2012). Arl13b in primary cilia regulates the migration and placement of interneurons in the developing cerebral cortex. Dev. Cell *23*, 925–938.

Higginbotham, H., Guo, J., Yokota, Y., Umberger, N.L., Su, C.Y., Li, J., Verma, N., Hirt, J., Ghukasyan, V., Caspary, T., et al. (2013). Arl13b-regulated cilia activities are essential for polarized radial glial scaffold formation. Nat. Neurosci. *16*, 1000–1007.

Hildebrandt, F., Benzing, T., and Katsanis, N. (2011). Ciliopathies. N. Engl. J. Med. *364*, 1533–1543.

Hilgendorf, K.I., Johnson, C.T., and Jackson, P.K. (2016). The primary cilium as a cellular receiver: organizing ciliary GPCR signaling. Curr. Opin. Cell Biol. *39*, 84–92.

Hippenmeyer, S., Vrieseling, E., Sigrist, M., Portmann, T., Laengle, C., Ladle, D.R., and Arber, S. (2005). A developmental switch in the response of DRG neurons to ETS transcription factor signaling. PLoS Biol. *3*, e159.

Hoshina, N., Tanimura, A., Yamasaki, M., Inoue, T., Fukabori, R., Kuroda, T., Yokoyama, K., Tezuka, T., Sagara, H., Hirano, S., et al. (2013). Protocadherin 17 regulates presynaptic assembly in topographic corticobasal ganglia circuits. Neuron *78*, 839–854.

Humbert, M.C., Weihbrecht, K., Searby, C.C., Li, Y., Pope, R.M., Sheffield, V.C., and Seo, S. (2012). ARL13B, PDE6D, and CEP164 form a functional network for INPP5E ciliary targeting. Proc. Natl. Acad. Sci. USA *109*, 19691–19696.

Idevall-Hagren, O., Dickson, E.J., Hille, B., Toomre, D.K., and De Camilli, P. (2012). Optogenetic control of phosphoinositide metabolism. Proc. Natl. Acad. Sci. USA *109*, E2316–E2323.

Jacoby, M., Cox, J.J., Gayral, S., Hampshire, D.J., Ayub, M., Blockmans, M., Pernot, E., Kisseleva, M.V., Compère, P., Schiffmann, S.N., et al. (2009). INPP5E mutations cause primary cilium signaling defects, ciliary instability and ciliopathies in human and mouse. Nat. Genet. *41*, 1027–1031.

Jansen, V., Alvarez, L., Balbach, M., Strünker, T., Hegemann, P., Kaupp, U.B., and Wachten, D. (2015). Controlling fertilization and cAMP signaling in sperm by optogenetics. eLife *4*, e05161.

Juric-Sekhar, G., Adkins, J., Doherty, D., and Hevner, R.F. (2012). Joubert syndrome: brain and spinal cord malformations in genotyped cases and implications for neurodevelopmental functions of primary cilia. Acta Neuropathol. *123*, 695–709.

Kalil, K., and Dent, E.W. (2014). Branch management: mechanisms of axon branching in the developing vertebrate CNS. Nat. Rev. Neurosci. *15*, 7–18.

Katsura, Y., Kubota, H., Kunida, K., Kanno, A., Kuroda, S., and Ozawa, T. (2015). An optogenetic system for interrogating the temporal dynamics of Akt. Sci. Rep. *5*, 14589.

Kholodenko, B.N. (2006). Cell-signalling dynamics in time and space. Nat. Rev. Mol. Cell Biol. *7*, 165–176.

Klapoetke, N.C., Murata, Y., Kim, S.S., Pulver, S.R., Birdsey-Benson, A., Cho, Y.K., Morimoto, T.K., Chuong, A.S., Carpenter, E.J., Tian, Z., et al. (2014). Independent optical excitation of distinct neural populations. Nat. Methods *11*, 338–346.

Kwon, C.H., Luikart, B.W., Powell, C.M., Zhou, J., Matheny, S.A., Zhang, W., Li, Y., Baker, S.J., and Parada, L.F. (2006). Pten regulates neuronal arborization and social interaction in mice. Neuron *50*, 377–388.

Lemmon, M.A., and Schlessinger, J. (2010). Cell signaling by receptor tyrosine kinases. Cell *141*, 1117–1134.

Madisen, L., Zwingman, T.A., Sunkin, S.M., Oh, S.W., Zariwala, H.A., Gu, H., Ng, L.L., Palmiter, R.D., Hawrylycz, M.J., Jones, A.R., et al. (2010). A robust and high-throughput Cre reporting and characterization system for the whole mouse brain. Nat. Neurosci. *13*, 133–140.

Manning, B.D., and Cantley, L.C. (2007). AKT/PKB signaling: navigating downstream. Cell *129*, 1261–1274.

Manning, B.D., and Toker, A. (2017). AKT/PKB signaling: navigating the network. Cell *169*, 381–405.

Mariani, L.E., Bijlsma, M.F., Ivanova, A.A., Suciu, S.K., Kahn, R.A., and Caspary, T. (2016). Arl13b regulates Shh signaling from both inside and outside the cilium. Mol. Biol. Cell *27*, 3780–3790.

Marley, A., and von Zastrow, M. (2012). A simple cell-based assay reveals that diverse neuropsychiatric risk genes converge on primary cilia. PLoS One *7*, e46647.

Mattila, P.K., and Lappalainen, P. (2008). Filopodia: molecular architecture and cellular functions. Nat. Rev. Mol. Cell Biol. *9*, 446–454.

McIntyre, J.C., Davis, E.E., Joiner, A., Williams, C.L., Tsai, I.C., Jenkins, P.M., McEwen, D.P., Zhang, L., Escobado, J., Thomas, S., et al. (2012). Gene therapy rescues cilia defects and restores olfactory function in a mammalian ciliopathy model. Nat. Med. *18*, 1423–1428.

Mejillano, M.R., Kojima, S., Applewhite, D.A., Gertler, F.B., Svitkina, T.M., and Borisy, G.G. (2004). Lamellipodial versus filopodial mode of the actin nanomachinery: pivotal role of the filament barbed end. Cell *118*, 363–373.

Miertzschke, M., Koerner, C., Spoerner, M., and Wittinghofer, A. (2014). Structural insights into the small G-protein Arl13B and implications for Joubert syndrome. Biochem. J. *457*, 301–311.

Mukhopadhyay, S., and Rohatgi, R. (2014). G-protein-coupled receptors, Hedgehog signaling and primary cilia. Semin. Cell Dev. Biol. *33*, 63–72.

Nachury, M.V., Seeley, E.S., and Jin, H. (2010). Trafficking to the ciliary membrane: how to get across the periciliary diffusion barrier? Annu. Rev. Cell Dev. Biol. *26*, 59–87.

Nguyen, T., and Di Giovanni, S. (2008). NFAT signaling in neural development and axon growth. Int. J. Dev. Neurosci. *26*, 141–145.

Nichols, A.S., Floyd, D.H., Bruinsma, S.P., Narzinski, K., and Baranski, T.J. (2013). Frizzled receptors signal through G proteins. Cell. Signal. *25*, 1468–1475.

Nishikimi, M., Oishi, K., and Nakajima, K. (2013). Axon guidance mechanisms for establishment of callosal connections. Neural Plast. *2013*, 149060.

Novarino, G., Akizu, N., and Gleeson, J.G. (2011). Modeling human disease in humans: the ciliopathies. Cell *147*, 70–79.

Omori, Y., Chaya, T., Yoshida, S., Irie, S., Tsujii, T., and Furukawa, T. (2015). Identification of G protein-coupled receptors (GPCRs) in primary cilia and their possible involvement in body weight control. PLoS One *10*, e0128422.

Oude Weernink, P.A., Han, L., Jakobs, K.H., and Schmidt, M. (2007). Dynamic phospholipid signaling by G protein-coupled receptors. Biochim. Biophys. Acta *1768*, 888–900.

Parisi, M.A. (2019). The molecular genetics of Joubert syndrome and related ciliopathies: the challenges of genetic and phenotypic heterogeneity. Transl. Sci. Rare Dis. *4*, 25–49.

Parisi, M., and Glass, I. (2019). Joubert Syndrome. In GeneReviews®, M.P. Adam, H.H. Ardinger, R.A. Pagon, S.E. Wallace, L.J.H. Bean, K. Stephens, and A. Amemiya, eds. (Seattle, WA: University of Washington, Seattle).

Parra, L.M., and Zou, Y. (2010). Sonic hedgehog induces response of commissural axons to semaphorin repulsion during midline crossing. Nat. Neurosci. *13*, 29–35.

Patro, R., Duggal, G., Love, M.I., Irizarry, R.A., and Kingsford, C. (2017). Salmon provides fast and bias-aware quantification of transcript expression. Nat. Methods *14*, 417–419.

Paxinos, G., and Franklin, K.B.J. (2001). The Mouse Brain in Stereotaxic Coordinates (Academic Press).

Phua, S.C., Chiba, S., Suzuki, M., Su, E., Roberson, E.C., Pusapati, G.V., Setou, M., Rohatgi, R., Reiter, J.F., Ikegami, K., et al. (2017). Dynamic remodeling of membrane composition drives cell cycle through primary cilia excision. Cell *168*, 264–279.e15.

Phua, S.C., Lin, Y.C., and Inoue, T. (2015). An intelligent nano-antenna: primary cilium harnesses TRP channels to decode polymodal stimuli. Cell Calcium *58*, 415–422.

Plotnikova, O.V., Seo, S., Cottle, D.L., Conduit, S., Hakim, S., Dyson, J.M., Mitchell, C.A., and Smyth, I.M. (2015). INPP5E interacts with AURKA, linking phosphoinositide signaling to primary cilium stability. J. Cell Sci. *128*, 364–372.

Poretti, A., Boltshauser, E., Loenneker, T., Valente, E.M., Brancati, F., Il'yasov, K., and Huisman, T.A.G.M. (2007). Diffusion tensor imaging in Joubert syndrome. AJNR Am. J. Neuroradiol. *28*, 1929–1933.

Puram, S.V., Kim, A.H., Ikeuchi, Y., Wilson-Grady, J.T., Merdes, A., Gygi, S.P., and Bonni, A. (2011). A CaMKIIbeta signaling pathway at the centrosome regulates dendrite patterning in the brain. Nat. Neurosci. *14*, 973–983.

Rafiullah, R., Long, A.B., Ivanova, A.A., Ali, H., Berkel, S., Mustafa, G., Paramasivam, N., Schlesner, M., Wiemann, S., Wade, R.C., et al. (2017). A novel homozygous ARL13B variant in patients with Joubert syndrome impairs its guanine nucleotide-exchange factor activity. Eur. J. Hum. Genet. *25*, 1324–1334.

Raper, J., and Mason, C. (2010). Cellular strategies of axonal pathfinding. Cold Spring Harbor Perspect. Biol. *2*, a001933.

Reiter, J.F., and Leroux, M.R. (2017). Genes and molecular pathways underpinning ciliopathies. Nat. Rev. Mol. Cell Biol. *18*, 533–547.

Romani, M., Micalizzi, A., and Valente, E.M. (2013). Joubert syndrome: congenital cerebellar ataxia with the molar tooth. Lancet Neurol. *12*, 894–905.

Sánchez-Alegría, K., Flores-León, M., Avila-Muñoz, E., Rodríguez-Corona, N., and Arias, C. (2018). PI3K signaling in neurons: a central node for the control of multiple functions. Int. J. Mol. Sci. *19*, 3725.

Sarkisian, M.R., and Guadiana, S.M. (2015). Influences of primary cilia on cortical morphogenesis and neuronal subtype maturation. Neuroscientist *21*, 136–151.

Sattar, S., and Gleeson, J.G. (2011). The ciliopathies in neuronal development: a clinical approach to investigation of Joubert syndrome and Joubert syndrome-related disorders. Dev. Med. Child Neurol. *53*, 793–798.

Sawano, A., Takayama, S., Matsuda, M., and Miyawaki, A. (2002). Lateral propagation of EGF signaling after local stimulation is dependent on receptor density. Dev. Cell *3*, 245–257.

Schmid, R.S., McGrath, B., Berechid, B.E., Boyles, B., Marchionni, M., Sestan, N., and Anton, E.S. (2003). Neuregulin 1-erbB2 signaling is required for the establishment of radial glia and their transformation into astrocytes in cerebral cortex. Proc. Natl. Acad. Sci. USA *100*, 4251–4256.

Schou, K.B., Pedersen, L.B., and Christensen, S.T. (2015). Ins and outs of GPCR signaling in primary cilia. EMBO Rep. *16*, 1099–1113.

Senocak, E.U., Oğuz, K.K., Haliloğlu, G., Topçu, M., and Cila, A. (2010). Structural abnormalities of the brain other than molar tooth sign in Joubert syndrome-related disorders. Diagn. Interv. Radiol. *16*, 3–6.

Siljee, J.E., Wang, Y., Bernard, A.A., Ersoy, B.A., Zhang, S., Marley, A., Von Zastrow, M., Reiter, J.F., and Vaisse, C. (2018). Subcellular localization of MC4R with ADCY3 at neuronal primary cilia underlies a common pathway for genetic predisposition to obesity. Nat. Genet. *50*, 180–185.

Spangler, S.M., and Bruchas, M.R. (2017). Optogenetic approaches for dissecting neuromodulation and GPCR signaling in neural circuits. Curr. Opin. Pharmacol. *32*, 56–70.

Stierl, M., Stumpf, P., Udwari, D., Gueta, R., Hagedorn, R., Losi, A., Gärtner, W., Petereit, L., Efetova, M., Schwarzel, M., et al. (2011). Light modulation of cellular cAMP by a small bacterial photoactivated adenylyl cyclase, bPAC, of the soil bacterium Beggiatoa. J. Biol. Chem. *286*, 1181–1188.

Su, C.Y., Bay, S.N., Mariani, L.E., Hillman, M.J., and Caspary, T. (2012). Temporal deletion of Arl13b reveals that a mispatterned neural tube corrects cell fate over time. Development *139*, 4062–4071.

Su, S., Phua, S.C., DeRose, R., Chiba, S., Narita, K., Kalugin, P.N., Katada, T., Kontani, K., Takeda, S., and Inoue, T. (2013). Genetically encoded calcium indicator illuminates calcium dynamics in primary cilia. Nat. Methods *10*, 1105–1107.

Thomas, S., Cantagrel, V., Mariani, L., Serre, V., Lee, J.E., Elkhartoufi, N., de Lonlay, P., Desguerre, I., Munnich, A., Boddaert, N., et al. (2015). Identification of a novel ARL13B variant in a Joubert syndrome-affected patient with retinal impairment and obesity. Eur. J. Hum. Genet. *23*, 621–627.

Umberger, N.L., and Caspary, T. (2015). Ciliary transport regulates PDGF-AA/αα signaling via elevated mammalian target of rapamycin signaling and diminished PP2A activity. Mol. Biol. Cell *26*, 350–358.

Vitriol, E.A., and Zheng, J.Q. (2012). Growth cone travel in space and time: the cellular ensemble of cytoskeleton, adhesion, and membrane. Neuron *73*, 1068–1081.

Wang, L., and Marquardt, T. (2013). What axons tell each other: axon-axon signaling in nerve and circuit assembly. Curr. Opin. Neurobiol. *23*, 974–982.

Wang, Z., Zhou, Y., Luo, Y., Zhang, J., Zhai, Y., Yang, D., Zhang, Z., Li, Y., Storm, D.R., and Ma, R.Z. (2015). Gene expression profiles of main olfactory epithelium in adenylyl cyclase 3 knockout mice. Int. J. Mol. Sci. *16*, 28320–28333.

Weimer, J.M., Stanco, A., Cheng, J.G., Vargo, A.C., Voora, S., and Anton, E.S. (2008). A BAC transgenic mouse model to analyze the function of astroglial SPARCL1 (SC1) in the central nervous system. Glia *56*, 935–941.

Welf, E.S., Ahmed, S., Johnson, H.E., Melvin, A.T., and Haugh, J.M. (2012). Migrating fibroblasts reorient directionality by a metastable, PI3K-dependent mechanism. J. Cell Biol. *197*, 105–114.

Winkle, C.C., Taylor, K.L., Dent, E.W., Gallo, G., Greif, K.F., and Gupton, S.L. (2016). Beyond the cytoskeleton: the emerging role of organelles and membrane remodeling in the regulation of axon collateral branches. Dev. Neurobiol. *76*, 1293–1307.

Yokota, Y., Ring, C., Cheung, R., Pevny, L., and Anton, E.S. (2007). Nap1-regulated neuronal cytoskeletal dynamics is essential for the final differentiation of neurons in cerebral cortex. Neuron *54*, 429–445.

Yu, T.W., and Bargmann, C.I. (2001). Dynamic regulation of axon guidance. Nat. Neurosci. *4*, 1169–1176.

Zhu, D., Shi, S., Wang, H., and Liao, K. (2009). Growth arrest induces primary-cilium formation and sensitizes IGF-1-receptor signaling during differentiation induction of 3T3-L1 preadipocytes. J. Cell Sci. *122*, 2760–2768.

STAR★METHODS

KEY RESOURCES TABLE

REAGENT or RESOURCE	SOURCE	IDENTIFIER
Antibodies		
Chicken polyclonal anti-GFP	Abcam	Cat# ab13970; RRID: AB_300798
Rabbit polyclonal anti-RFP	Rockland	Cat# 600-401-379; RRID: AB_2209751
Rabbit polyclonal anti-Caspase 3	Millipore	Cat# ab3623; RRID: AB_91556
Mouse monoclonal anti-Arl13b	NeuroMabs	Cat# 75-287; RRID: AB_11001586
Goat polyclonal anti-ACIII	Santa Cruz	Cat# 32114; RRID: AB_2305175
Rabbit monoclonal anti-HA Tag	Invitrogen	Cat# 71-5500; RRID: AB_2533988
Mouse monoclonal anti-Tau	Millipore	Cat# MAB3420; RRID: AB_94855
Chicken polyclonal anti-Map2	Abcam	Cat# ab5392; RRID: AB_2138153
AlexaFluor goat anti-mouse 488	Invitrogen	Cat#A32723; RRID: AB_2633275
AlexaFluor goat anti-mouse Cy3	Invitrogen	Cat# A10521; RRID: AB_2534030
AlexaFluor goat anti-mouse 647	Invitrogen	Cat# A21235; RRID: AB_2535804
AlexaFluor goat anti-rabbit 488	Invitrogen	Cat# A11034; RRID: AB_2576217
AlexaFluor goat anti-rabbit Cy3	Invitrogen	Cat# A10520; RRID: AB_2534029
AlexaFluor goat anti-rabbit 647	Invitrogen	Cat# A32733; RRID: AB_2633282
AlexaFluor goat anti-chicken 488	Invitrogen	Cat#A11039; RRID: AB_2534096
AlexaFluor goat anti-chicken 647	Invitrogen	Cat#A21449; RRID: AB_2535866
Chemicals, Peptides, and Recombinant Proteins		
DAPI	Sigma-Aldrich	Cat# D9542
ATP	Sigma-Aldrich	Cat# FLAAS-1VL
Clozapine N-oxide (CNO)	Sigma-Aldrich	Cat# C0832-5MG
DMSO	Sigma-Aldrich	Cat# D2438-50ML
Deposited Data		
RNA-seq data	This paper	GEO database (GSE120310)
Experimental Models: Cell Lines		
HEK293T	ATCC	CRL-3216
IMCD3	ATCC	CRL-2123
MEF (Arl13b$^{hnn/hnn}$)	Caspary et al., 2007	N/A
Experimental Models: Organisms/Strains		
Mouse: Arl13b$^{hnn/+}$	Dr. Tamara Caspary; Caspary et al., 2007	N/A
Mouse: Arl13b$^{Lox/Lox}$	Dr. Tamara Caspary; Su et al., 2012	N/A
Mouse: Inpp5e^{rdg}	Dr. Tamara Caspary; Su et al., 2012	MGI: 6295836
Mouse: Inpp5e$^{Lox/Lox}$	Jacoby et al., 2009	N/A
Mouse: Ift88$^{tm1.1Bky}$	Haycraft et al., 2007	MGI: 3710186
Mouse: B6.Cg-Gt(ROSA)26Sor$^{tm3(CAG-EYFP)Hze}$/J	The Jackson Laboratory	JAX: 007903
Mouse: B6.Cg-Gt(ROSA)26Sor$^{tm9(CAG-tdTomato)Hze}$/J	The Jackson Laboratory	JAX: 007909
Mouse: Neurod6$^{tm1(cre)Kan}$	Goebbels et al., 2006	MGI: 2668659
Mouse: B6.Cg-Gt(ROSA)26So$^{rtm9(CAG-tdTomato)Hze/}$J	The Jackson Laboratory	JAX: 007909
Recombinant DNA		
Plasmid: pAAV-DIO-EF1a-mCherry-2a-hARL13B (WT)	Guo et al., 2017	N/A
Plasmid: pAAV-DIO-EF1a-mCherry-2a-hARL13B (R79Q)	Guo et al., 2017	N/A
Plasmid: pAAV-DIO-EF1a-mCherry-2a-hARL13B (W82X)	Guo et al., 2017	N/A
Plasmid: pAAV-DIO-EF1a-mCherry-2a-hARL13B (Y86C)	Guo et al., 2017	N/A
Plasmid: pAAV-DIO-EF1a-mCherry-2a-hARL13B (R200C)	Guo et al., 2017	N/A

(*Continued on next page*)

Continued

REAGENT or RESOURCE	SOURCE	IDENTIFIER
Plasmid: pAAV-DIO-EF1a-mCherry-2a-hARL13B (G75R)	This paper	N/A
Plasmid: pAAV-DIO-EF1a-mCherry-2a-mArl13b (mV358A)	Guo et al., 2017	N/A
Plasmid: Cilia-GFP (IA-GFP)	Dr. Takanari Inoue; Su et al., 2013	N/A
Plasmid: Cilia-GECO1.0 (IA-G-GECO.1)	Dr. Takanari Inoue; Su et al., 2013	N/A
Plasmid: Cilia-GECO1.0 (IA-R-GECO.1)	Dr. Takanari Inoue; Su et al., 2013	N/A
Plasmid: Cilia-hM3D$_q$ (*cilia targeting sequence: c terminal of fibrocystin*)	Guo et al., 2017; Follit et al., 2010	N/A
Plasmid: pCAG-Cre	Addgene	Cat#13775
Plasmid: pCAG-GFP	Addgene	Cat#16664
Plasmid: CIBN-GFP	Idevall-Hagren et al., 2012	N/A
Plasmid: CRY2-iSH2	Idevall-Hagren et al., 2012	N/A
Plasmid: mCh-CRY2-iSH2	Idevall-Hagren et al., 2012	N/A
Plasmid: mCherry-CRY2-5Ptase$_{INPP5E}$	Idevall-Hagren et al., 2012	N/A
Plasmid: CRY2-5Ptase$_{INPP5E}$	Idevall-Hagren et al., 2012	N/A
Plasmid: RFP-PH$_{AKT}$	Addgene	Cat#51465
Plasmid: mCh-PH$_{GRPI}$	Idevall-Hagren et al., 2012	N/A
Plasmid: Cilia-CIBN-GFP (*cilia targeting sequence: IA*)	This paper; Su et al., 2013	N/A
Plasmid: CRY2-venus-AKT1	Katsura et al., 2015	N/A
Plasmid: mCh-CRY2-AKT1	This paper	N/A
Plasmid: Cilia-bPAC (*cilia targeting sequence: Sstr3*)	Jansen et al., 2015	N/A
Plasmid: pAAV-DIO-FLAG-GPR88*	Siljee et al., 2018	N/A
Plasmid: Pcdh17-GFP	Hayashi et al., 2014	N/A
AAV5-Synapsin-tdTomato	Klapoetke et al., 2014	UNC viral vector core.
Software and Algorithms		
GraphPad	NA	https://www.graphpad.com/scientific-software/prism/
Excel	NA	https://products.office.com/en-us/excel
ImageJ	NA	https://imagej.nih.gov/ij/
Zeiss LSM Image Browser	NA	https://www.zeiss.com/microscopy/us/website/downloads/lsm-image-browser.html

LEAD CONTACT AND MATERIALS AVAILABILITY

Further information and requests for resources and reagents should be directed to, and will be fulfilled by the Lead Contact, E.S. Anton (anton@med.unc.edu).

EXPERIMENTAL MODEL AND METHOD DETAILS

Mice

This study is based on data from mice at various developmental stages (embryonic days 16, 18, postnatal days 1, 7, 30, and 60) and includes both males and females. Mice were cared for according to animal protocols approved by the University of the North Carolina. Arl13b or Inpp5e was conditionally inactivated in cortical projection neurons and deep cerebellar nuclei by crossing *Arl13b$^{Lox/Lox}$* mice (Arl13b^{tm1Tc}, MGI: 4948239) (Su et al., 2012) or *Inpp5e$^{Lox/Lox}$* (Inpp5e^{tm1Ssch}, MGI:4360185) (Jacoby et al., 2009) with Nex-Cre mice (Goebbels et al., 2006). Further, transgenic mice carrying the Tau-Lox-STOP-Lox-GFP cassette (Hippenmeyer et al., 2005) or Ai9 reporter (Madisen et al., 2010) were bred into the *Arl13b$^{Lox/+}$*; *Nex-Cre* and *Inpp5e$^{Lox/+}$; Nex-Cre* lines. Cre recombination of the *Tau-Lox-STOP-Lox-mGFP* or Ai9 transgene leads to GFP or mRFP expression, respectively, in the processes of all Cre-positive neurons. *Arl13b$^{Lox/+}$; Nex-Cre* or *Inpp5e$^{Lox/+}$; Nex-Cre* littermates served as controls. Arl13b null mice (*Arl13b$^{-/-}$* or *Arl13b^{hnn}*; MGI:3578151), Ift88 null mice (Ift88$^{tm1.1Bky}$, MGI: 3710186), Inpp5e^{M2} mice (MGI: 5296378) were generated as described in Caspary et al. (2007); Haycraft et al. (2007); and Su et al. (2012), respectively. All lines were genotyped as previously described (Caspary et al., 2007; Su et al., 2012; Higginbotham et al., 2013). Location of different anatomical regions of the mouse brain were annotated using the mouse brain atlas (Paxinos and Franklin, 2001).

DNA Constructs

CIBN-GFP, CRY2-iSH2, mCh-CRY2-iSH2, mCherry-CRY2-5Ptase$_{INPP5E}$, CRY2-5Ptase$_{INPP5E,}$ RFP-PH$_{AKT}$, and mCh-PH$_{GRPI}$ (Idevall-Hagren et al., 2012) are gifts from Dr. Pietro De Camilli, Yale University. The cilia targeted CIBN-GFP was generated by replacing R-GECO1.0 in IA-R-GECO1.0 with CIBN-GFP. IA-R-GECO1.0 (Su et al., 2013) is a gift from Dr. Takanari Inoue, John Hopkins University. CRY2-Venus-AKT1 (Katsura et al., 2015) is a gift from Dr. Takeaki Ozawa (the University of Tokyo). mCh-CRY2-AKT1 was generated by replacing 5Ptase$_{INPP5E}$ with AKT1 in mCherry-CRY2-5Ptase$_{INPP5E}$. The cilia-targeted bPAC (cilia-bPAC) (Jansen et al., 2015) is a gift from Dr. Dagmar Wachten (Center of Advanced European Studies and Research, Bonn, Germany). pAAV-DIO-FLAG-GPR88* (Siljee et al, 2018) is a generous gift from Dr. Christian Vaisse (the University of California, San Francisco). Pcdh17-GFP (Hayashi et al., 2014) is a generous gift from Dr. Masatoshi Takeichi (Riken Center for Developmental Biology). The Cre-inducible adeno-associated virus (AAV) vectors expressing ARL13B variants and mCherry were generated as described previously (Guo et al., 2017). The AAV5-Synapsin-tdTomato virus (Klapoetke et al., 2014) was obtained from UNC viral vector core.

CLARITY Imaging

CLARITY experiments were performed based on protocols available at: http://wiki.claritytechniques.org/index.php/Solutions. Briefly, *Arl13b$^{Lox/lox}$-NexCre-Ai9* and control pups (P1) were perfused with ice cold 4% PFA. Brains with spinal cords attached were dissected and post fixed in 4% PFA overnight at 4°C, followed by incubation in 30ml hydrogel solution for 2 days at 4°C. Following polymerization of the hydrogel monomers, samples were incubated with clearing solution for 2 weeks at 37°C. Cleared samples were washed with PBST (0.1% TritonX in 1× PBS) buffer for 2 days and stored in PBST at 4°C. For CLARITY imaging, samples were incubated with 85% glycerol for 1hrs, placed in a glass bottom FluoroDIsh chambers (World Precision Instruments, Inc.) filled with 85% glycerol and imaged using a Zeiss780 confocal microscope equipped with 10× objectives.

Microfluidic Chamber Assay

Microfluidic chambers (Higginbotham et al., 2012) were attached to laminin coated glass coverslips. 5μl containing 200-K cells from DCN of P3 *Arl13b$^{Lox/+}$; NexCre* or *Arl13b$^{Lox/Lox}$; NexCre* brains electroporated with BFP (Addgene #127348) plasmids were seeded onto one side of the microfluidic chamber. 24 hours later, the same number of cells from P3 *Arl13b$^{Lox/+}$; NexCre*; *Ai9* or *Arl13b$^{Lox/Lox}$; NexCre; Ai9* brains electroporated with Pcdh17-EGFP were seeded onto the opposite chamber. Cells were maintained at 37°C/5% CO2 and 10μl of new media (DMEM/N2/B27) was added every 24 hours. After 48 hours, cells were fixed in 4% paraformaldehyde and analyzed for the expression pattern of Pcdh17-EGFP at BFP$^+$/tdTom$^+$ axon-axon contacts.

In Utero Electroporation

Lateral ventricles of *Arl13b$^{Lox/+}$* and *Arl13b$^{Lox/Lox}$*, or *Inpp5e$^{Lox/+}$* and *Inpp5e$^{Lox/Lox}$* (E15.5) embryos were electroporated as described previously (Guo et al., 2015; Higginbotham et al., 2012). Briefly, 1μl of CAG-Cre (Addgene #13775) and CAG-GFP (Addgene #16664) plasmid DNA (2 μg/μl) was injected into the lateral ventricles of E15.5 brains and electroporated using 5 pulses at 30 V for 50 ms at 950-ms intervals through the uterine wall using a BTX ElectroSquarePorator (ECM 830). Embryos were then allowed to develop *in vivo* and analyzed at P1 or P21. Plasmids used for *in utero* electroporation were prepared using the EndoFree Plasmid kit (Qiagen).

Primary Neuronal Culture and Transfection

Deep cerebellar nuclei (P2) or dorsal cortices (E15) were dissected in Hank's buffered salt solution (HBSS), dissociated in HBSS containing papain (Worthington) and DNase I (100 mg/ml, Sigma) for 10 min at 37C, washed in HBSS three times and manually triturated in Neural basal medium supplemented with DNase I. Neurons from E11.5 or 12.5 cortices were similarly processed. Neurons were transfected using Amaxa^{TM}Nuleofector^{TM} II kit (Lonza) or Invitrogen Lipofectamine 2000 reagent according to the manufacturer's protocol. 1.0 × 10^4 cells were plated per 35-mm glass bottom dish (MatTek) coated with poly-L-lysine /laminin (Sigma) and cultured for 1–4 days in Neurobasal-A /5% B27/1% GlutaMAX/1% P/S media.

Chemogenetic Manipulation of Ciliary Signaling and Axonal Imaging

Cultured DCN neurons were transfected with R-GECO1.0 and Cilia-hM3D$_q$ and imaged at an acquisition rate of 0.5 Hz using a Zeiss 780 live cell confocal microscope. The effects of CNO or DMSO on axonal Ca^{2+} and growth cone behavior were assessed in neurons expressing ciliary hM3D$_q$ by recording upto 20min before and 20min after addition. GECO1.0 fluorescence intensity values were normalized against background and the average baseline values were measured prior to CNO or DMSO addition. Image analysis was performed using Zeiss LSM Image Browser or ImageJ software.

Optogenetic Manipulation of Ciliary-PI3K/AKT, Ciliary-Adenylyl Cyclase Signaling, and Axonal Imaging

For ciliary-PI3K activation, cultured DCN neurons were transfected with Cilia-GFP-CIBN, mCh-CRY2-iSH2, or CRY2-iSH2. For ciliary-AKT activation, DCN neurons were transfected with Cilia-GFP-CIBN, mCh-CRY2-AKT1, or CRY2-Venus-AKT1. For ciliary-Inpp5e$_{5ptase}$ activation, DCN neurons were transfected with Cilia-GFP-CIBN and mCh-CRY2-5ptase-Inpp5e. RFP-PH$_{AKT}$ or mCh-PH$_{GRPI}$ were used as PIP3 sensors. For ciliary-bPAC activation, DCN neurons were transfected with mCh-Sstr3-bPAC and pcDNA3.1-BFP. A train of 200-ms blue laser light (488nm) focused on primary cilia for upto 3 minutes was used to induce dimerization between CRY2 and CIBN within primary cilia (Idevall-Hagren et al., 2012). Growth cone morphology and dynamics were imaged with 561-nm laser (mCh or mRFP) at an acquisition rate of 0.5 Hz upto 20min before and 20min after photo-activation using a Zeiss 780 live

cell confocal microscope. The imaging positions and parameters for primary ciliary light activation and growth cone imaging was setup using the multi-position, time series, and photo bleaching applications in ZEN software.

Immunohistochemistry

Cerebral cortical sections and neurons were immunolabeled as previously described (Guo et al., 2017; Schmid et al., 2003; Weimer et al., 2008; Yokota et al., 2007) with the following primary antibodies: anti-GFP (chicken, 1:1000; Abcam, ab13970), anti-RFP (rabbit, 1:500; Rockland, cat. Nr. 600-401-379), anti-ACIII (rabbit polyclonal, 1:100; Santa Cruz, sc-56855), anti-Tau (mouse 1:1000, Millipore, MAB3420), anti-Map2 (chicken polyclonal, 1:1000, Abcam, ab5392), immunoreactivity was detected by incubation with appropriate AlexaFluor 488 or Cy3-conjugated secondary antibodies (Invitrogen and Jackson ImmunoResearch). AlexaFluor 488, 647 or Cy3-conjugated (Invitrogen and Jackson ImmunoResearch) secondary antibodies were used. Nuclei were counterstained with DAPI (Sigma).

Tissue Culture and Transfection

Mouse embryonic fibroblast (MEF) cells were derived from wild type and *Arl13b*$^{-/-}$ E12.5 embryos as previously described (Higginbotham et al., 2012). MEF cells and IMCD3 (authenticated by American Type Culture Collection [ATCC]) were grown in DMEM/ F12 media supplemented with 10% fetal bovine serum (FBS) and 1% penicillin/streptomycin (P/S) at 37°C/5% CO_2. Cells were allowed to reach 80% confluency and ciliogenesis was induced by serum starvation for 24 hours. Cells were then transfected using Invitrogen Lipofectamine 2000 reagent according to manufacture's instructions.

Immunoblotting

Cortices of Arl13b null and control embryos (E12) or cultured cells were harvested in 200-μl cell lysis buffer (Cell signaling, #9803) with protease and phosphatase inhibitor cocktail (Thermo Scientific). The lysates were briefly sonicated and centrifuged at 14,000 rpm for 20 min at 4°C. Protein concentrations were determined using the protein assay reagent (Bio-Rad). Samples were mixed with 3× SDS sample buffer and boiled for 5 min. Samples were then resolved in SDS-polyacrylamide gels, transferred to nitrocellulose, and incubated with following primary antibodies: rabbit anti-pAKT [Thr308] (1:1000, Cell signaling, #9275), rabbit anti-pGSK3β (1:1000, Cell signaling, #9331), rabbit anti-pS6 (1:1000, Cell signaling, #4858), rabbit anti-AKT (1:1000, Cell signaling, #9272), mouse anti-β-actin (1:1000, Abcam, ab8226). Immunoblots were developed using horseradish peroxidase-conjugated goat anti-mouse or goat anti-rabbit IgG, followed by detection with enhanced chemiluminescence.

RNA-Seq

RNA was isolated *from E12.5 control and Arl13b*$^{-/-}$ *cortices* with the RNeasy plus mini kit (Cat. #74134, Qiagen). RNA yield and quality was determined with a NanoDrop 1000 Spectrophotometer (Thermo Scientific). RNA quality was further assessed by an Agilent Bioanalyzer 2100 to obtain a RNA integrity number (RIN). RIN values exceeding 8 were used for sequencing. RNA samples were used to generate and barcode cDNA libraries using the Nugen ovation RNAseq Plus Kit at the UNC High Throughput Sequencing Facility. Pool of 6 samples were sequenced in a single lane in a HiSeq 4000 sequencer (Illumina) using 50 bp paired-end reads.

Image Analysis

All images were analyzed using ImageJ (NIH) and Zeiss Zen. Kymographs and fluorescence intensity of Ca^{2+} sensors RFP-GECO1.0 or IA-GFP-GECO1.0, and PIP3 sensors RFP-PH_{AKT} or mCh-PH_{GRPI} were quantified using ImageJ (Guo et al., 2017). ROIs located in cilia, soma, or growth cones of neurons were selected and the mean value of fluorescence intensity of ROIs (after background subtraction) over time was plot profiled. For the turning angle measurement of SCP, lines were drawn along the SCP tract pre- and post turning and the turning angle was quantified using the angle tool in ImageJ.

RNA-Seq Data Analysis

Reads were filtered for quality using the FASTX toolkit's fastq_quality_filter (http://hannonlab.cshl.edu/fastx_toolkit/index.html) with 90% of the bases having a minimal quality score of 20. Sequencing adaptors were trimmed using cutadapt. Reads were aligned to the mm9 reference genome using STAR. Transcript abundance was estimated using Salmon (Patro et al., 2017). DESeq2 was used to normalize read depth and calculate differential gene expression. Genes with a Benjamini-Hochberg (B&H) FDR adjusted p-value < 0.05, fold change > 2 or <-2 were considered significant. GO term annotation of gene lists was performed using ToppGene. GO terms with a B&H FDR adjusted p-value < 0.05 were considered significant. Lists of significant GO terms were clustered using REVIGO. Ingenuity Pathway Analysis (IPA) [https://www.qiagenbioinformatics.com/ products/ingenuity-pathway-analysis] was used for pathway analysis, novel network identification, and upstream regulator analysis.

QUANTIFICATION AND STATISTICAL ANALYSIS

General Statistical Analysis

GraphPad or Excel was used for data analysis. Two-tailed Student's t test and ANOVA were performed using GraphPad. No *a priori* power analyses were performed, but sample sizes were similar to those described in previous related studies (Guo et al., 2015, 2017;

Higginbotham et al., 2012, 2013). All experiments were independently repeated for at least 3 or more times. All data are expressed as means ± standard error of the mean (SEM). Statistical details, including p values, are indicated in text or figure legends.

DATA AND CODE AVAILABILITY

The published article includes all datasets generated or analyzed during this study. RNA-seq data were deposited in the GEO database (GSE120310).

Developmental Cell, Volume *51*

Supplemental Information

Primary Cilia Signaling Promotes Axonal Tract Development and Is Disrupted in Joubert Syndrome-Related Disorders Models

Jiami Guo, James M. Otis, Sarah K. Suciu, Christy Catalano, Lei Xing, Sandii Constable, Dagmar Wachten, Stephanie Gupton, Janice Lee, Amelia Lee, Katherine H. Blackley, Travis Ptacek, Jeremy M. Simon, Stephane Schurmans, Garret D. Stuber, Tamara Caspary, and E.S. Anton

Supplemental Figures

Figure S1 (Related to Figures 1, 2, 3, and 4)**: Cortical projection and deep cerebellar nuclei neurons are ciliated.** (A-D) $tdTom^{+}$ cortical projection (A, B) or deep cerebellar nuclei (C, D) neurons from control *Arl13b$^{lox/+}$; NexCre; Ai9* brains at P1 (A, C) and P30 (B, D) were immunostained with anti-ACIII antibodies. 3 brains per age group were analysed. * indicates location of neurons. DCN, deep cerebellar nuclei. Scale bar, 10μm.

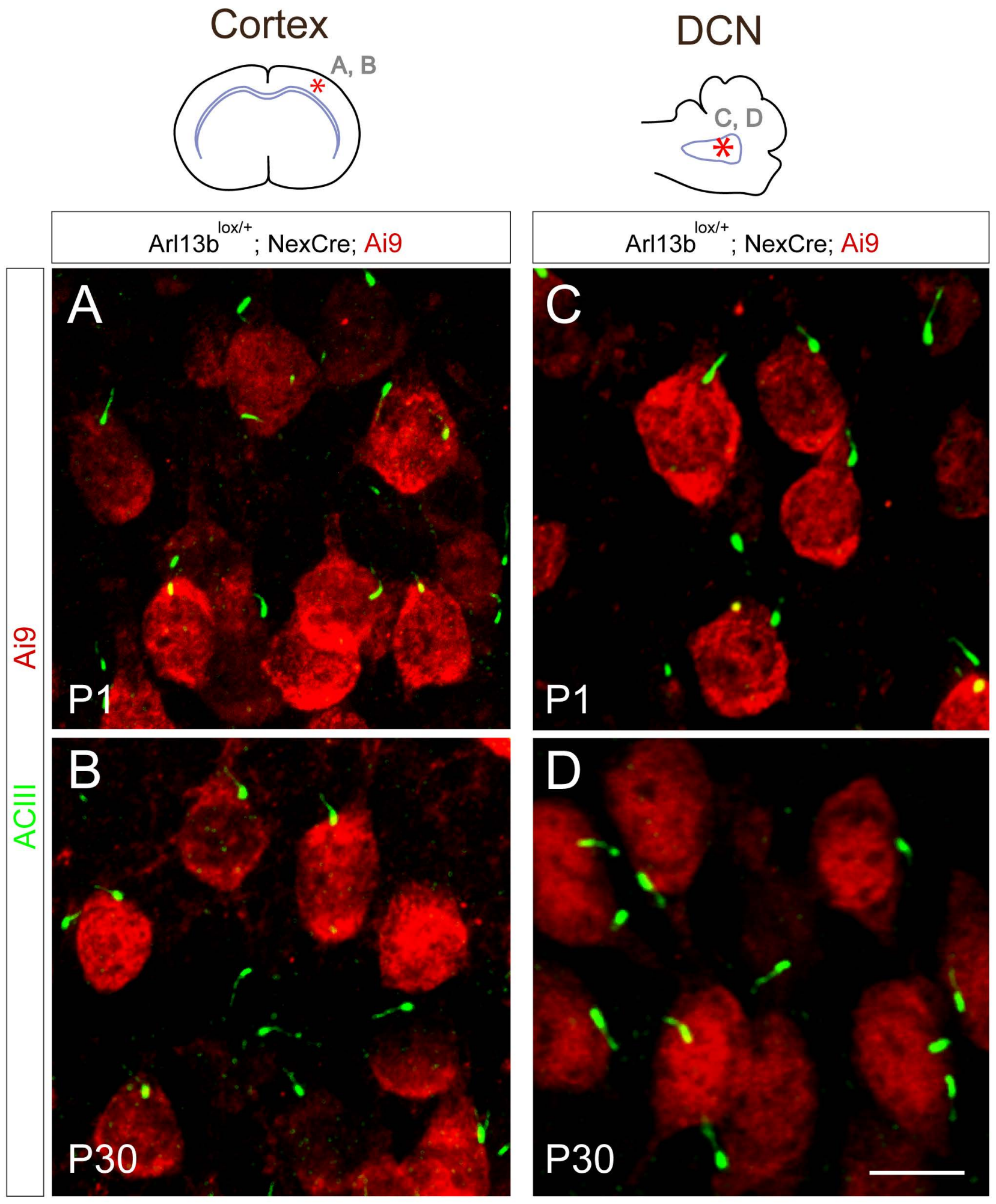
Cortex
A, B
DCN
C, D
Arl13b lox/+ ; NexCre; Ai9
Arl13b lox/+ ; NexCre; Ai9
A
C
P1
P1
B
D
P30
P30
Ai9
ACIII

Figure S2 (Related to Figures 1 and 2)**: Deletion of *Arl13b* did not increase cell death of DCN or cortical neurons.** Cerebellar (A, B) or cortical (C, D) sections of *Arl13b*$^{lox/+}$*; NexCre; Ai9* (A, C) and *Arl13b*$^{lox/lox}$*; NexCre; Ai9* (B, D) brains (P1) were immunostained with anti-Caspase3 antibody. DCN is outlined with dotted lines (A, B). (A', B') Higher magnification of the outlined region in A and B. White arrowheads point to representative tdTom^{+}/Caspase^{+} neurons. **(**E) Quantification of tdTom^{+}/Caspase^{+} cells in DCN and cortex, respectively. Data shown are mean ± SEM. (Student's *t*-test, $p_{[DCN]}$= 0.61; $p_{[Cortex]}$= 0.15. n=4 brains). DCN, deep cerebellar nuclei. Scale bar, 166μm (A, B); 85μm (C, D).

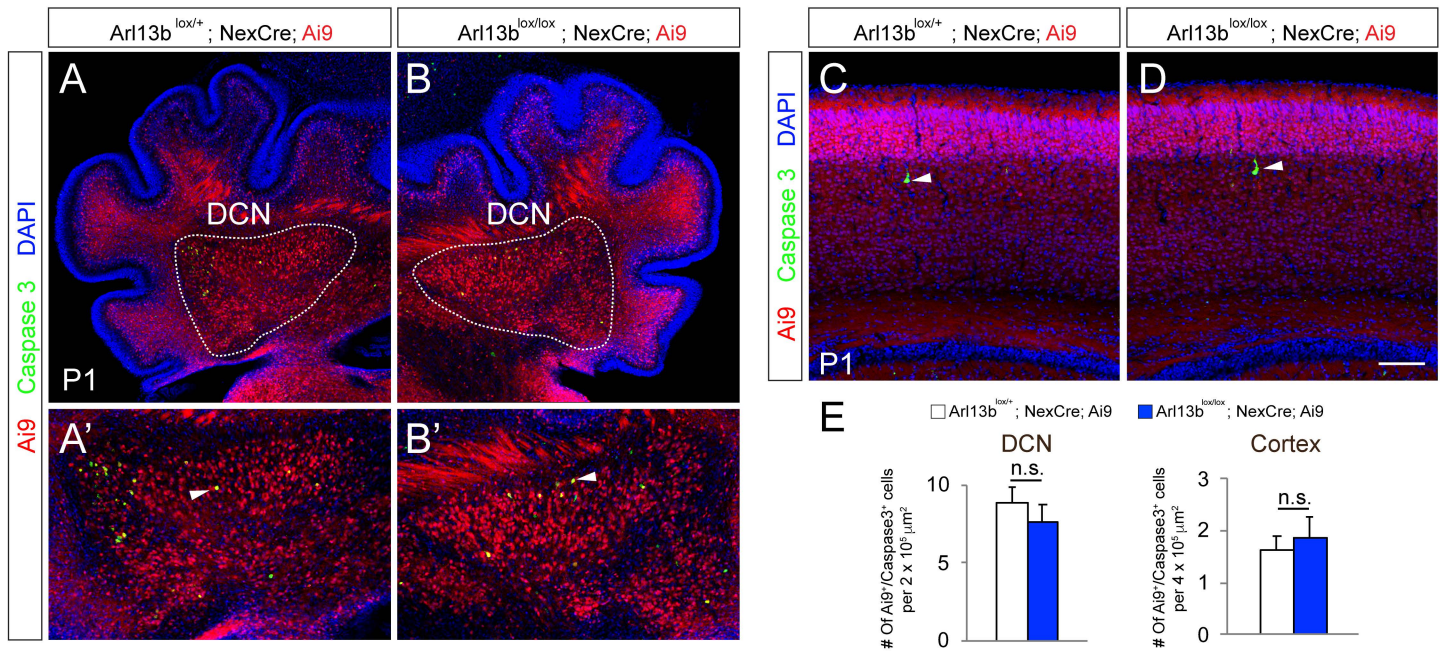
Arl13b lox/+ ; NexCre; Ai9
Arl13b lox/lox ; NexCre; Ai9
A
B
DCN
DCN
P1
DAPI
Caspase 3
Ai9
A'
B'
C
D
E
n.s.
DCN
Cortex
Of Ai9+/Caspase3+ cells per 2 x 10^5 µm^2
Of Ai9+/Caspase3+ cells per 4 x 10^5 µm^2
10
5
0
3
2
1

Figure S3 (Related to Figures 1 and 2)**: Deletion of *Arl13b* leads to axonal tract defects.** (A, B) GFP^+ SCP axonal labeling in *Arl13b$^{lox/+}$; NexCre; Taustop* (A) and *Arl13b$^{lox/lox}$; NexCre; Taustop* (B) brains (E16) show diffused outgrowth of SCP in Arl13b cKO when compared to control. Panels A' and B' show higher magnification images of the outlined areas in A and B. (C, D) GFP labeling in sagittal brain sections (P1) show diffused SCP outgrowth in Arl13b cKO. (E, F) Increased turning angle of SCP tract in Arl13b cKO. Data shown are mean ± SEM. $^*P<0.05$ (Student's *t*-test, p= 0.0002, n=3 brains). (G, H) Disorganized axons of transverse pontine tract in Arl13b cKO (arrow, H). CB, cerebellum; DCN, deep cerebellar nuclei; SCP, superior cerebellar peduncle. Scale bar, 100μm (A, B); 355μm (C, D); 220μm (E, F); 135μm (G, H, I, J).

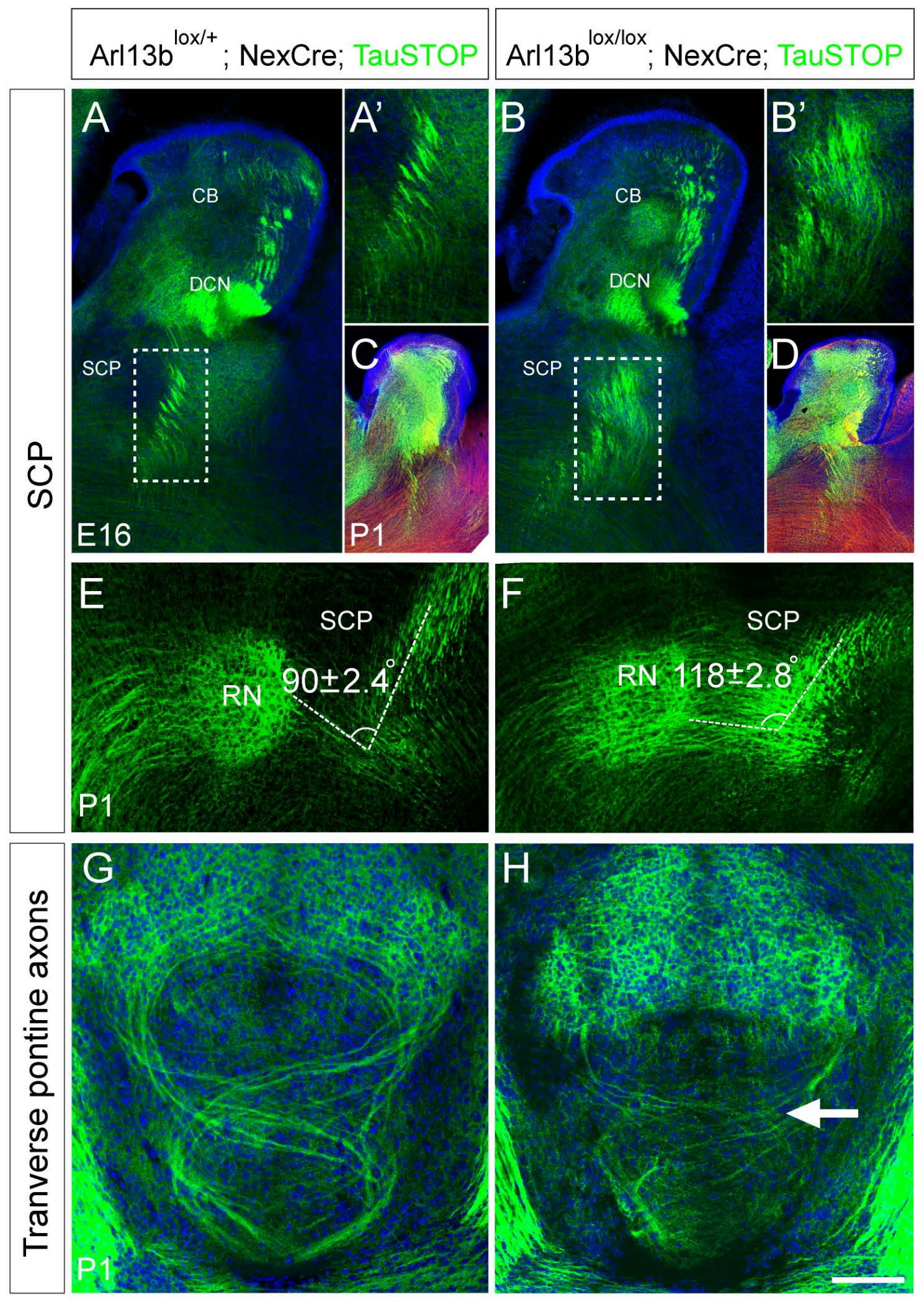
Arl13b lox/+ ; NexCre; TauSTOP
Arl13b lox/lox ; NexCre; TauSTOP
SCP
A
A'
B
B'
CB
DCN
SCP
C
D
E16
P1
E
F
SCP
RN
90±2.4°
118±2.8°
P1
Tranverse pontine axons
G
H
P1

Figure S4 (Related to Figure 3)**: Normal axon-dendrite polarization of Arl13b deficient neurons.** Axons and dendrites in DCN neurons dissociated from *Arl13b*$^{lox/+}$*; NexCre; Ai9* (A) and *Arl13b*$^{lox/lox}$*; NexCre; Ai9* (B) brains (P2) were immunolabeled with anti-Tau and anti-Map2 antibodies, respectively, after 48 hours *in vitro*. 22 neurons from 3 brains per group were analysed. Scale bar, 12μm (A, B).

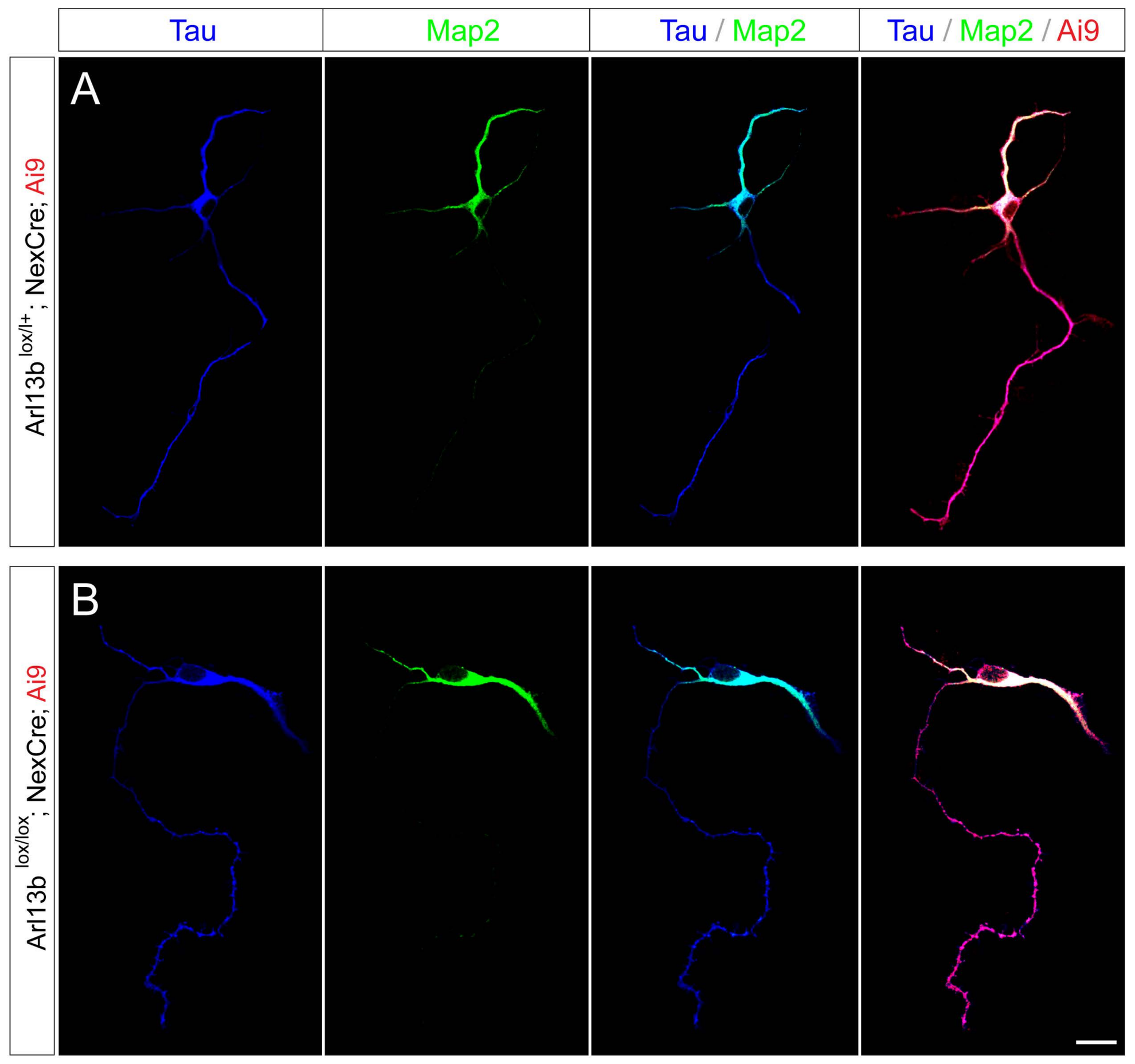
Tau
Map2
Tau / Map2
Tau / Map2 / Ai9
A
Arl13b lox/l+; NexCre; Ai9
B
Arl13b lox/lox; NexCre; Ai9

Figure S5 (Related to Figures 3 and 4)**: Deletion of *Arl13b* leads to axonal growth defects *in vitro*.** (A-D) Cultured cortical neurons from control, *Arl13b*$^{-/-}$ (A) and *Ift88*$^{-/-}$ (B) cortices (E11.5) were analyzed at different time points as indicated. Red arrowheads point to the primary axonal branching points. (C, D) Quantification of axonal outgrowth after 72 hours *in vitro*. Data shown are mean ± SEM. $^{*}P<0.05$ (Student's *t*-test, $p_{[C,\ Length\ of\ primary\ axon]} = 0.08$, $p_{[C,\ \#\ of\ primary\ axonal\ branches]} = 6.4E\text{-}05$, $p_{[D,\ Length\ of\ primary\ axon]} = 0.07$, $p_{[D,\ \#\ of\ primary\ axonal\ branches]} = 1.8E\text{-}05$; n=12 neurons). (E) Representative axonal growth cones from control, *Arl13b*$^{-/-}$, and *Ift88*$^{-/-}$ cortices. Red arrowheads point to aberrantly long filopodial extensions. (F) Quantification of axonal growth cone (GC) area, GC filopodia length, and growth cone filopodia/lamellipodia ratio. Data shown are mean ± SEM. $^{*}P<0.05$ (Student's *t*-test, $p_{[GC\ area\ ctrl\ vs.\ Arl13b]} = 0.004$, $p_{[GC\ area\ ctrl\ vs.\ Ift88]} = 0.004$, $p_{[Length\ of\ GC\ filopodia,\ ctrl\ vs.\ Arl13b]} = 1.0E\text{-}05$, $p_{[Length\ of\ GC\ filopodia,\ ctrl\ vs.\ Ift88]} = 0.0009$, $p_{[GC\ filopodia/lamellipodia\ ratio,\ ctrl\ vs.\ Arl13b]} = 2.1E\text{-}04$, $p_{[GC\ filopodia/lamellipodia\ ratio,\ ctrl\ vs.\ Ift88]} = 3.4E\text{-}04$; n=28 cells). Scale bar, 20μm (A, B); 8.5μm (E).

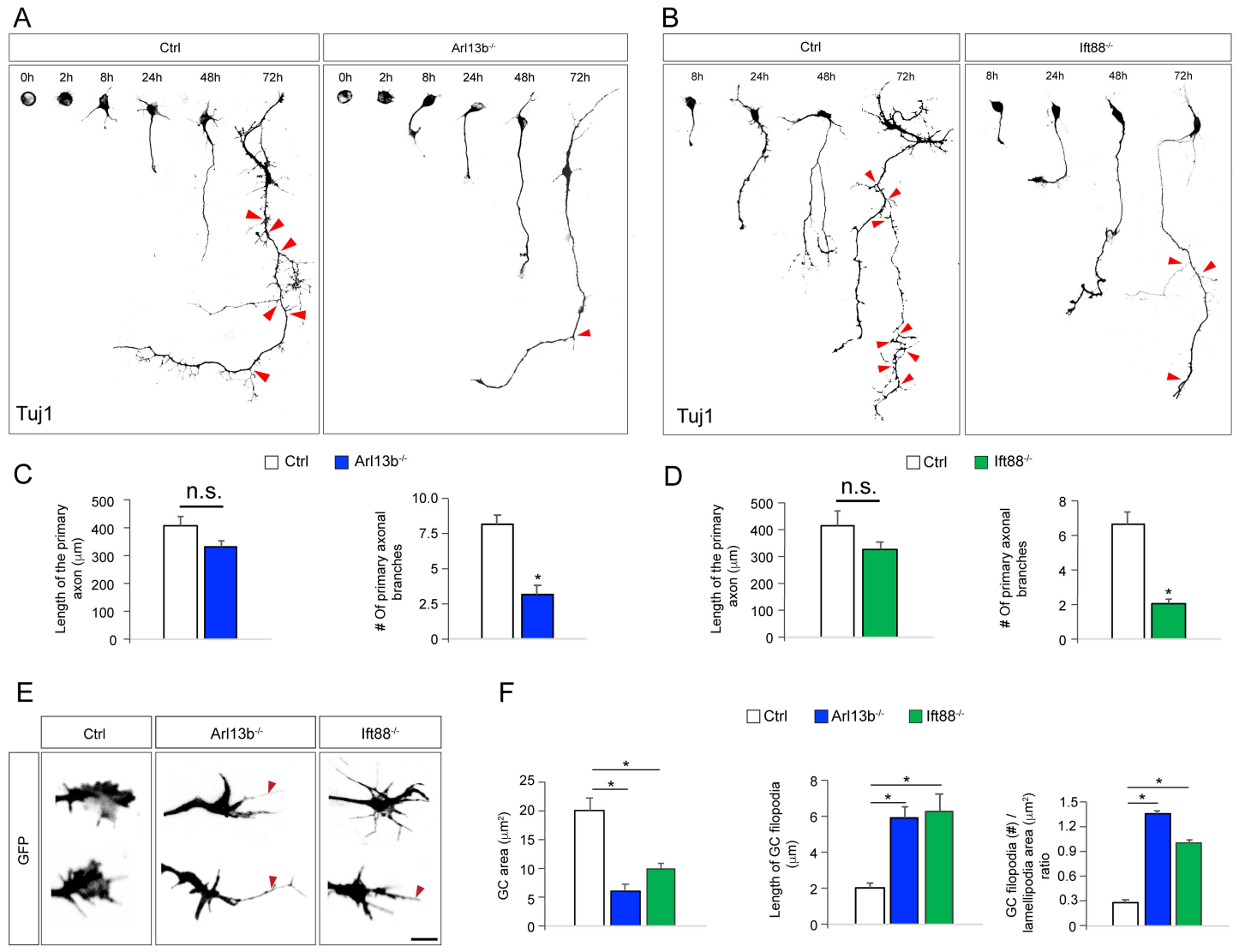
A
Ctrl
Arl13b-/-
0h
2h
8h
24h
48h
72h
Tuj1
B
Ctrl
Ift88-/-
8h
24h
48h
72h
Tuj1
C
Ctrl
Arl13b-/-
n.s.
Length of the primary axon (µm)
500
400
300
200
100
0
Of primary axonal branches
10.0
7.5
5
2.5
0
*
D
Ctrl
Ift88-/-
n.s.
Length of the primary axon (µm)
500
400
300
200
100
0
Of primary axonal branches
8
6
4
2
0
*
E
Ctrl
Arl13b-/-
Ift88-/-
GFP
F
Ctrl
Arl13b-/-
Ift88-/-
GC area (µm2)
25
20
15
10
5
0
*
*
Length of GC filopodia (µm)
8
6
4
2
0
*
*
GC filopodia (#) / lamellipodia area (µm2) ratio
1.5
1.2
0.9
0.6
0.3
0
*
*

Figure S6 (Related to Figures 5 and 6)**: Deletion of Arl13b or Inpp5e in developing neurons leads to increased PI3K/AKT activity.** (A-C) DCN neurons from *NexCre; Ai9* (Ctrl; A), *Arl13b$^{lox/lox}$; NexCre; Ai9* (Arl13b cKO; B), and *Inpp5e$^{lox/lox}$; NexCre; Ai9* (Inpp5e cKO; C) brains were transfected with PIP3 biosensor RFP-PH_{AKT}. Primary cilia were immunolabeled with anti-ACIII antibodies. White arrows and arrowheads point to primary cilia in control and Arl13b cKO or Inpp5e cKO neurons, respectively. White dashed lines outline the primary cilium. (D, E) Quantification of RFP-PH_{AKT} intensity along primary cilia (D) and across neuronal soma (E). Data shown are mean ± SEM. $^{*}P$<0.05 (Student's *t*-test, $p_{[D\ Ctrl\ vs.\ Arl13b\ cKO]}$ = 6.2E-05, $p_{[D\ Ctrl\ vs.\ Inpp5e\ cKO]}$ =4.2E-05, $p_{[E,\ soma,\ Ctrl\ vs.\ Arl13b\ cKO]}$ =0.003, $p_{[E,\ soma,\ Ctrl\ vs.\ Inpp5e\ cKO]}$ = 0.008, $p_{[E,\ plasma\ membrane,\ Ctrl\ vs.\ Arl13b\ cKO]}$ =2.2E-04, $p_{[E,\ plasma\ membrane,\ Ctrl\ vs.\ Inpp5e\ cKO]}$ = 3.1E-04, n=16 neurons). (F) Average RFP-PH_{AKT} intensity normalized to total ciliary area (μm^2). Data shown are mean ± SEM. $^{*}P$<0.05 (Student's *t*-test, $p_{[Ctrl\ vs.\ Arl13b\ cKO]}$ = 3.9E-05, $p_{[Ctrl\ vs.\ Inpp5e\ cKO]}$ =4.8E-05, n=16 neurons). (G-L) Cortical neurons (E12.5) from Control (G, I) and *Arl13b$^{-/-}$* cortices (H, J) were transfected with PIP3 biosensors, RFP-PH_{AKT} or mCh-PH_{GRPI}. Primary cilia were immunolabeled with anti-ACIII antibodies. White arrows and arrowheads point to primary cilia in control and Arl13b$^{-/-}$ neurons, respectively. (K, L) Quantification of the average ciliary RFP-PH_{AKT} (K) and mCh-PH_{GRPI} (L) fluorescence intensity in primary cilia. Data shown are mean ± SEM. $^{*}P$<0.05 (Student's *t*-test, $p_{[J]}$ = 1.2E-08, $p_{[K]}$ =3.2E-09). (M) Control and *Arl13b$^{-/-}$* or Inpp5e^{rdg} (E12.5) cortical lysates were immunoblotted for p-AKT (T308), p-GSK3β, p-S6, p-CREB (S133), total AKT, and β-actin. (N) Quantification of immunoblots. Data shown are mean ± SEM. $^{*}P$<0.05 (Student's *t*-test, $p_{[p\text{-}AKT]Arl13b}$ = 0.003, $p_{[p\text{-}GSK3_{\beta}]Arl13b}$ =2.4E-04; $p_{[p\text{-}S6]Arl13b}$ =0.008, $p_{[p\text{-}CREB]Arl13b}$ = 0.002, $_{[p\text{-}AKT]Inpp5e}$ = 0.001, $p_{[p\text{-}GSK3_{\beta}]Inpp5e}$ =1.4E-03; $p_{[p\text{-}S6]Inpp5e}$ =4.1E-03, $p_{[p\text{-}CREB]Inpp5e}$ = 0.009, n=3 experiments). Scale bar, 6μm (A-C, G-J).

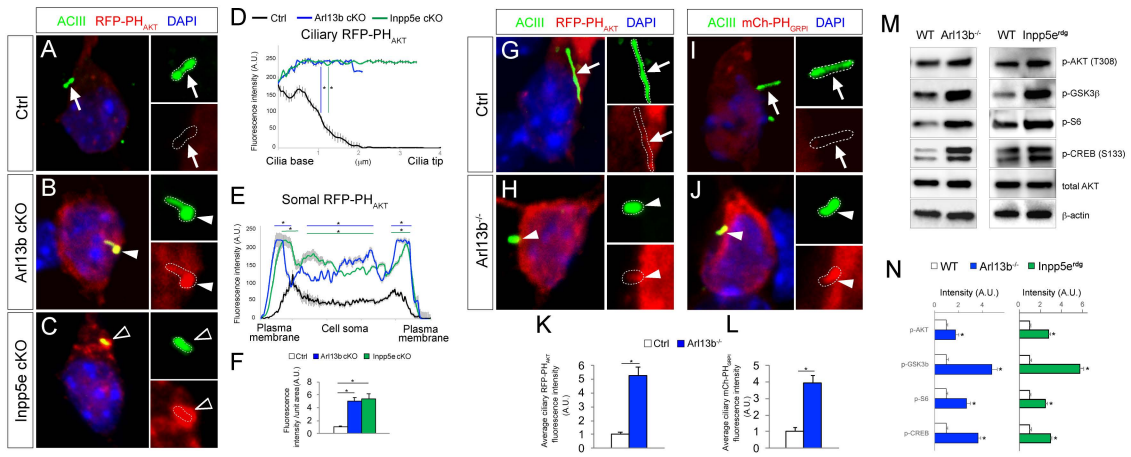
ACIII RFP-PHAKT DAPI
Ctrl
Arl13b cKO
Inpp5e cKO
A
B
C
D
Ctrl
Arl13b cKO
Inpp5e cKO
Ciliary RFP-PHAKT
Fluorescence intensity (A.U.)
Cilia base
(μm)
Cilia tip
E
Somal RFP-PHAKT
Plasma membrane
Cell soma
Plasma membrane
F
Fluorescence intensity /unit area(A.U.)
ACIII RFP-PHAKT DAPI
ACIII mCh-PHGRPI DAPI
G
H
I
J
K
Average ciliary RFP-PHAKT fluorescence intensity (A.U.)
L
Average ciliary mCh-PHGRPI fluorescence intensity (A.U.)
M
WT
Arl13b-/-
Inpp5erdg
p-AKT (T308)
p-GSK3β
p-S6
p-CREB (S133)
total AKT
β-actin
N
Intensity (A.U.)
p-AKT
p-GSK3b
p-S6
p-CREB

Figure S7 (Related to Figure 6)**: Control, non-selective optogenetic manipulations of ciliary or somal PI3K signaling do not change axonal behavior.** (A, B) No changes in axon growth cone morphology were seen after ciliary blue light illumination in DCN neurons expressing Cilia-GFP and CRY2-iSH2. Here, the absence of ciliary CIBN prevents iSH2 recruitment to cilium and thus the lack of effect. (B) Quantification of growth cone morphology. Data shown are mean ± SEM. (Student's *t*-test, p>0.05, n=24 neurons). (C, D) No changes in growth cone morphology were seen in DCN neurons expressing Cilia-CIBN-GFP and CRY2-iSH2 after ciliary illumination with non-specific 568nm wavelength laser. 488nm (blue light) wavelength laser is necessary to induce CIBN-CRY2 interaction and ciliary activation. (D) Quantification of growth cone morphology. Data shown are mean ± SEM. (Student's *t*-test, p>0.05, n=16 neurons). (E, F) No changes in growth cone morphology were seen after non-ciliary blue light activation of a comparable size region of the soma in DCN neurons expressing regular CIBN-GFP and CRY2-iSH2. (F) Quantification of growth cone morphology. Data shown are mean ± SEM. (Student's *t*-test, p>0.05, n=26 neurons). (G, H) No changes in growth cone morphology were seen after ciliary blue light illumination of DCN neurons expressing Cilia-CIBN-GFP and CRY2-iSH2 in the presence of p-AKT inhibitor, LY294002 (10μM) or actin polymerization inhibitor, Latrunculin B (1μM). Quantification of growth cone morphology. Data shown are mean ± SEM. (Student's *t*-test, p>0.05, n=12 neurons). Also shown are kymographs of PIP3 sensor mCh-PH_{GRPI} intensity in axonal growth cones before and after ciliary activation of PI3K. t' in panel A, C, E, G, and H includes 20 seconds to move from growth cone (pre-light activation) to primary cilia or soma, photo-activation (3 mins.) and 18-20 seconds to move back to growth cone (post-light activation). Scale bar, 5μm (A, C, E); 8.5μm (G, H).

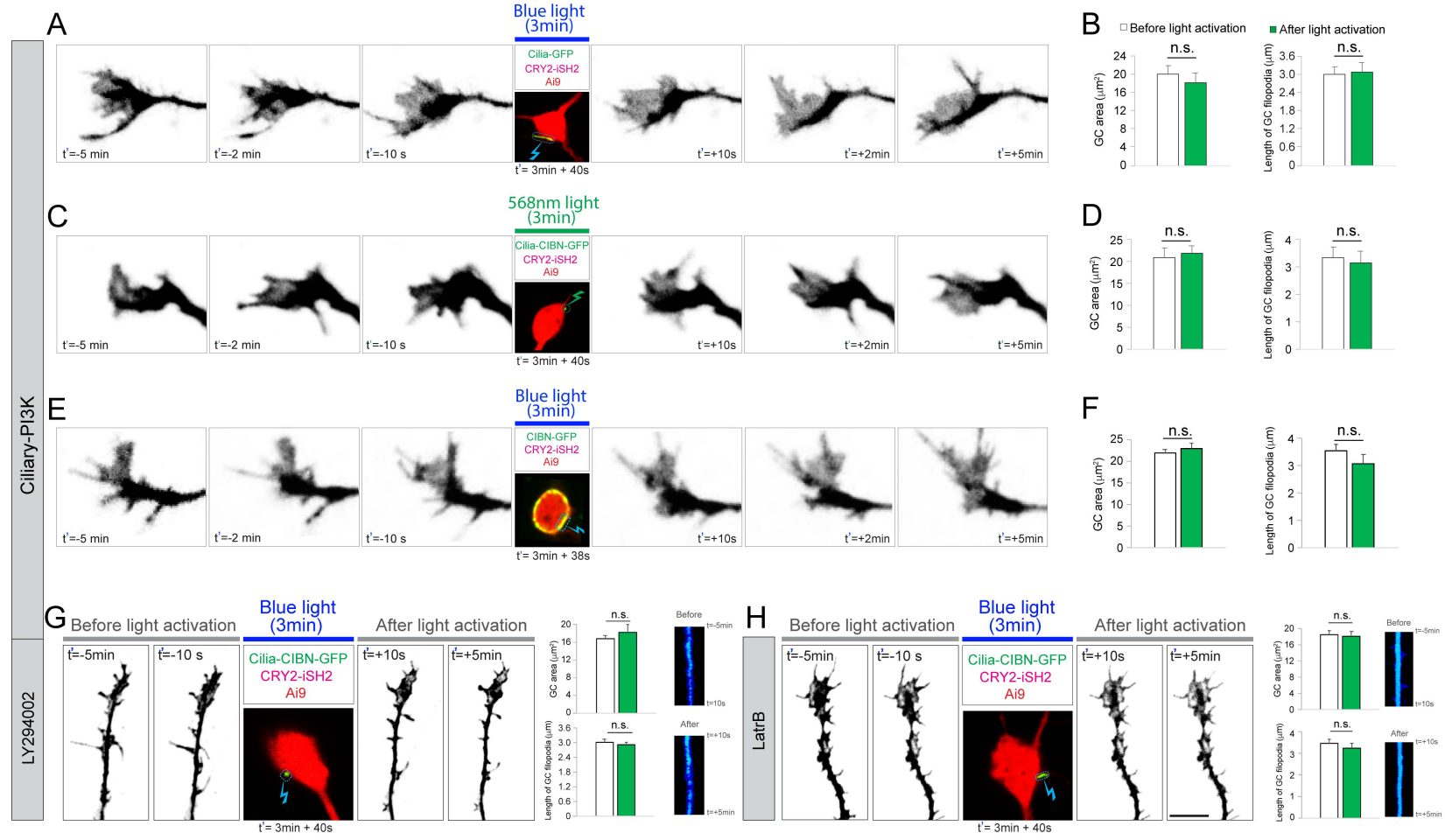
Ciliary-PI3K
LY294002
LatrB
A
Blue light (3min)
Cilia-GFP
CRY2-iSH2
Ai9
t'=-5 min
t'=-2 min
t'=-10 s
t'= 3min + 40s
t'=+10s
t'=+2min
t'=+5min
B
Before light activation
After light activation
n.s.
GC area (μm²)
Length of GC filopodia (μm)
C
568nm light (3min)
Cilia-CIBN-GFP
CRY2-iSH2
Ai9
D
E
Blue light (3min)
CIBN-GFP
CRY2-iSH2
Ai9
t'= 3min + 38s
F
G
Before light activation
Blue light (3min)
After light activation
t'=-5min
t'=-10 s
Cilia-CIBN-GFP
CRY2-iSH2
Ai9
t'=+10s
t'=+5min
t'= 3min + 40s
Before
After
t=-5min
t=+10s
t=+5min
H

Figure S8 (Related to Figures 1-6)**: Altered transcriptional landscape after *Arl13b* deletion.** (A) Heatmap of RNAseq data from control and *Arl13b*$^{-/-}$ cortices (E12.5). FDR < 0.05, n= 3 embryos. (B) Representative, significant GO terms (Biological process) are clustered and shown using REVIGO. Axonal related GO terms are highlighted in red. (C) IPA-based gene-gene network (Cellular Development, Tissue Development, Cell-To-Cell Signaling and Interaction) of differentially expressed genes in *Arl13b*$^{-/-}$ brains.

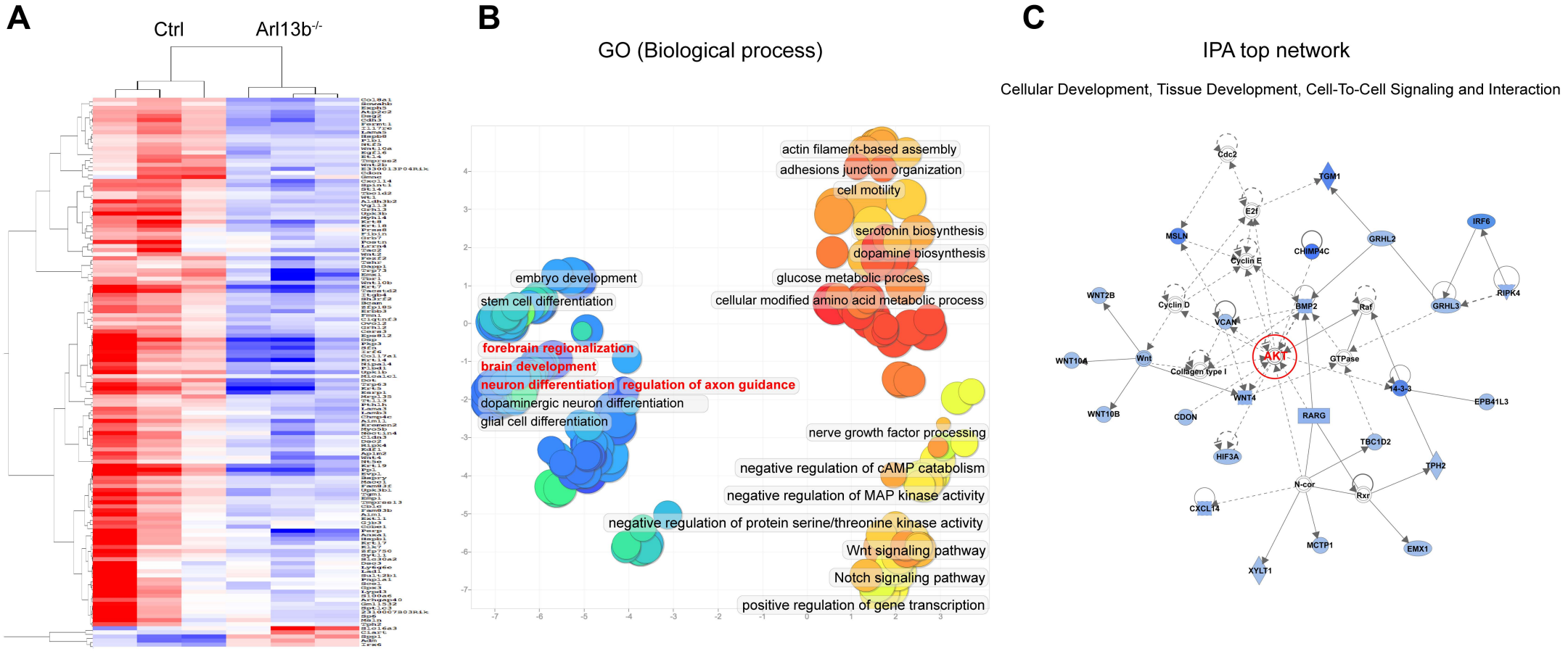
A
Ctrl
Arl13b-/-
B
GO (Biological process)
actin filament-based assembly
adhesions junction organization
cell motility
serotonin biosynthesis
dopamine biosynthesis
glucose metabolic process
cellular modified amino acid metabolic process
embryo development
stem cell differentiation
forebrain regionalization
brain development
neuron differentiation
regulation of axon guidance
dopaminergic neuron differentiation
glial cell differentiation
nerve growth factor processing
negative regulation of cAMP catabolism
negative regulation of MAP kinase activity
negative regulation of protein serine/threonine kinase activity
Wnt signaling pathway
Notch signaling pathway
positive regulation of gene transcription
C
IPA top network
Cellular Development, Tissue Development, Cell-To-Cell Signaling and Interaction
Cdc2
TGM1
E2f
MSLN
CHIMP4C
GRHL2
IRF6
Cyclin E
WNT2B
Cyclin D
BMP2
Raf
GRHL3
RIPK4
VCAN
WNT10A
Wnt
AKT
GTPase
Collagen type I
14-3-3
EPB41L3
WNT4
WNT10B
CDON
RARG
HIF3A
TBC1D2
TPH2
N-cor
Rxr
CXCL14
MCTP1
EMX1
XYLT1